

## Article

# Effect of Dissolved Carbon Dioxide on Cavitation in a Circular Orifice

Sina Safaei \* and Carsten Mehring

Institute of Mechanical Process Engineering, Böblinger Str. 72, 70199 Stuttgart, Germany; carsten.mehring@imvt.uni-stuttgart.de

\* Correspondence: sina.safaei@imvt.uni-stuttgart.de

**Abstract:** In this work, we investigate the effect of dissolved gas concentration on cavitation inception and cavitation development in a transparent sharp-edged orifice, similar to that previously analyzed by Nurick in the context of liquid injectors. The working liquid is water, and carbon dioxide is employed as a non-condensable dissolved gas. Cavitation inception points are determined for different dissolved gas concentration levels by measuring wall-static pressures just downstream of the orifice contraction and visually observing the onset of a localized (vapor) bubble cloud formation and collapse. Cavitation onset correlates with a plateau in wall-static pressure measurements as a function of a cavitation number. An increase in the amount of dissolved carbon dioxide is found to increase the cavitation number at which the onset of cavitation occurs. The transition from cloud cavitation to extended-sheet or full cavitation along the entire orifice length occurs suddenly and is shifted to higher cavitation numbers with increasing dissolved gas content. Volume flow rate measurements are performed to determine the change in the discharge coefficient with the cavitation number and dissolved gas content for the investigated cases. CFD analyses are carried out based on the cavitation model by Zwart et al. and the model by Yang et al. to account for non-condensable gases. Discharge coefficients obtained from the numerical simulations are in good agreement with experimental values, although they are slightly higher in the cavitating case. The earlier onset of fluid cavitation (i.e., cavitation inception at higher cavitation numbers) with increasing dissolved carbon dioxide content is not predicted using the employed numerical model.

**Keywords:** cavitation number; cavitation inception; outgassing; dissolved carbon dioxide; discharge coefficient



**Citation:** Safaei, S.; Mehring, C. Effect of Dissolved Carbon Dioxide on Cavitation in a Circular Orifice. *Fluids* **2024**, *9*, 41. <https://doi.org/10.3390/fluids9020041>

Academic Editors: Ashwin Vaidya and Rui Han

Received: 6 November 2023

Revised: 22 January 2024

Accepted: 30 January 2024

Published: 1 February 2024



**Copyright:** © 2024 by the authors. Licensee MDPI, Basel, Switzerland. This article is an open access article distributed under the terms and conditions of the Creative Commons Attribution (CC BY) license (<https://creativecommons.org/licenses/by/4.0/>).

## 1. Introduction

When the pressure  $p$  in a liquid falls below a certain threshold or critical pressure  $p_{crit}$ , vapor bubbles are generated [1–3]. This abrupt phase-change process, which is associated with the generation of noise and vibration in the system, is called cavitation or, more precisely, vapor cavitation. When the pressure drop is a result of pressure reduction due to an acceleration of the liquid, the cavitation phenomenon is referred to as hydrodynamic cavitation. On the other hand, pressure reduction in a liquid can also result in a degassing process, i.e., the evolution of gases previously dissolved in the liquid phase. This process is frequently referred to as gas cavitation. Vapor cavitation can have severe adverse effects on the processes within which it occurs. For instance, on the efficiency and service life of ship propellers and hydrofoils, since it causes disturbances of the flowfield around the propeller blades and foils, energy dissipation, and the collapse of the generated vapor bubbles (once they reach areas of higher pressure in the flow) can significantly damage the blade/foil surfaces and lead to material erosion or failure. The cavitation phenomenon has also found broad technical applications. Acoustic cavitation (where pressure variations are induced via ultrasonication) is used to erode and break kidney stones [4] or to clean the surfaces of root canals, filter membranes, surgical equipment, or electronic substrates [5].

Hydrodynamic cavitation has found applications in water purification, the recycling of waste, and process water and material recycling [6–10]. As gases dissolved in the liquid phase evolve, they can affect cavitation inception [11,12] and the subsequent dynamics of the cavitation bubbles, including, for example, peak pressures during a bubble collapse. Control of this latter and other parameters using the amount of dissolved gas present in the liquid phase can be used in cavitation reactors [13] to control the cleaning action exerted on dispersed matter present within the liquid phase or treat its surface in a controlled way.

The present investigation aims to provide additional information on the influence of dissolved gases on cavitation onset by systematically varying the dissolved gas (i.e., CO<sub>2</sub>) fluid content for a well-known orifice flow case [14]. The newly obtained experimental results augment the fairly small database on orifice cavitation in the presence of dissolved gases, improving the ability to test and validate new cavitation models, which include the effect of non-condensable gases on hydrodynamic cavitation.

### 1.1. Experimental Studies on Orifice Cavitation

Prediction and/or sensing of cavitation inception is an important topic for operational safety (w.r.t process performance and system hardware failure) [15] and its promotion or control in related applications. Observing the onset of cavitation and its transition to fully cavitating flow in simple hydrodynamic systems has also been a useful benchmark case for evaluating the accuracy of CFD analysis tools used for the design of hydrodynamic cavitation reactors or other processes where cavitation phenomena play an important role. Nurick [14] was one of the first to study cavitation in straight cylindrical sharp-edged orifices, specifically in context with their relevance to so-called unlike (fuel-oxidizer) impinging doublet injector elements for rocket propulsion. Nurick measured static pressures at two locations in close vicinity and downstream of the contraction as a function of orifice inlet pressure (at fixed downstream pressure). He also provided flow visualizations for a nozzle made of Lucite (PMMA), visualizing the cavitation region from the onset of cavitation to full cavitation. However, Nurick did not investigate the effect of dissolved gases in his work. Nurick's early contribution to the topic remains a frequently used benchmark for CFD-based cavitation models, even though he later also investigated flow transition (from non-cavitating to cavitating flow) for other geometries, e.g., in a 90-degree sharp-edge orifice [16].

The effect of dissolved gas on the onset of cavitation in a liquid flowing through an orifice was already discussed by Yan and Thorpe [17] and later investigated by Mishra and Peles [18]. They found that cavitation inception occurred at higher values of cavitation numbers with increasing amounts of oxygen dissolved in the liquid. They also observed a faster transition between cavitation onset and full cavitation with increasing dissolved oxygen content (see also Nurick [16] in this context). On the other hand, the dissolved gas content did not have an effect on the discharge coefficient in their experiments. The influence of dissolved gas content on hydrodynamic cavitation was also considered by Zhang, Zuo, and Liu [19], finding only little influence of the dissolved gas (oxygen) content on the (mean) length of the cavitation zone downstream of the ramp.

Li, Gu, and Chen [11] studied the influence of dissolved gases on the tensile strength of liquids and cavitation inception under acoustic cavitation conditions. They found that with increased gas concentration (nitrogen or oxygen), the tensile strength of water decreases, whereby the effect is stronger for oxygen in comparison to nitrogen as dissolved gas. The effect of dissolved gases on liquid cavitation has also been analyzed by Rooze [20], focusing on radical production in ultrasonic cavitation. The author also analyzed hydrodynamic cavitation for a similar configuration as Misha and Peles [18] but limited to the range of full cavitation without including dissolved gases. Freudigmann et al. [21] and Kowalski et al. [22] studied the evolution of dissolved gases out of the liquid phase as a result of vapor cavitation. The latter authors identify three regimes for cavitation-induced gas release with an exponential increase in evolved gas volume fraction with a decreasing cavitation number at high cavitation intensities.

Duke et al. [23–25] presented a series of papers investigating cavitating nozzle flow via X-ray radiography with and without dissolved gases. In order to determine the vapor and evolved gas phase fractions, they doped the liquid phase in [24] with an X-ray fluorescent bromine tracer and substituted the dissolved air with krypton. They observed that vapor cavitation is found only in an annular wall region beginning at the edge of the contraction. For the case of dissolved gas, they found a core region with increased, evolved gas content and a reduction in the true vapor cavitation zone. The latter is explained by the appearance of gas bubbles (appearing prior to vapor cavitation), thereby displacing the cavitation zones that would otherwise appear at the respective locations. In [25], the authors use a nozzle with a similar geometry as in [24] but slightly different transition sections. In addition, the nozzle is made of beryllium alloy, whereas in prior investigations, polycarbonate plastic nozzles were used. Quantitative measurements were provided for (total) vapor distribution, area concentration, and discharge coefficients for a broad range of Reynolds numbers and cavitation numbers and for the case with and without dissolved nitrogen in the liquid phase. Selected results were compared to those obtained previously under the same operating conditions for nozzles made of plastic. In the latter case, the authors found considerable amounts of vapor/gas in the center region of the constriction for the case with dissolved gas but not for the case without dissolved gas (see above). However, for the same case with a beryllium alloy nozzle, no differences were found between the cases with and without dissolved gas (nitrogen) present. The authors attributed this difference to gas evolving out of the liquid phase at imperfections on the nozzle walls in the case of the plastic material, which is not found in the nozzles made of beryllium. The authors found that the physical area contraction coefficient (i.e., the ratio of liquid flow area and geometric area) is independent of the amount of dissolved gas in the beryllium nozzle but decreases slightly when moving from the degassed to dissolved gas (i.e., nitrogen) condition in case of the plastic nozzle. The discharge coefficients of either the nozzle, plastic, or beryllium alloy were not affected by the amount of dissolved gases in the liquid and were found to follow the Nurick solution for sharp-edged orifices. For the plastic nozzle, this suggests that the evolving gas displaces the cavitation voids rather than the liquid phase such that the void distribution and velocity field yield the same effective discharge. Measurements on the effect of dissolved gas content on the onset of cavitation were not provided by Duke et al. [25].

### *1.2. Numerical Studies on Orifice Cavitation and the Effect of Dissolved Gases on Cavitation*

Cavitating flows pertain to the class of multiphase flows with a mass transfer between the phases, namely evaporation (vapor cavitation) and condensation. If the liquid phase contains non-dissolved gases, this gas can also evolve out of or re-dissolve into the liquid phase, thereby impacting the cavitation phenomena. Numerous physical and mathematical models were developed to describe the multiphase flow and the phase-transition/change aspects of cavitating flows. The approaches for modeling multiphase flows can be categorized based on how the various phases are being described and the type of equations that are being solved for each phase, namely the Euler–Lagrange (see, for example [26]) and the Euler–Euler approach.

In the latter case, both liquid and vapor phases are considered as interpenetrating continua for which proper field or transport equations are being solved. Here, one distinguishes between mixture models, interface-tracking models, and multifluid Eulerian models.

Within multifluid Eulerian models, momentum and continuity equations are being solved for each phase while they share the same pressure field. The interaction between each phase depends on the type of phase involved and phase concentrations.

In mixture models, the various phases are considered to be a single continuous mixture. Proper transport equations for the mixture and continuity equations for the dispersed phases are solved together with algebraic equations for the relative velocities between the dispersed phase(s) and the continuous phase. In the homogeneous mixture model, no slip exists between the phases. In interface-tracking methods such as volume of fluid (VOF)

or level-set (LS) methods, the phase transport (of all the phases) is solved using a single momentum equation, while the interface between the phases is tracked explicitly.

For the modeling of the mass transfer between the phases, the most frequently employed (macroscopic) models pertain to two major groups, i.e., equation of state (EOS) models and bubble dynamics models.

The latter group calculates the rate of mass transfer based on bubble dynamics governed using the Rayleigh–Plesset (R–P) equation or a modified form of the RP equation (without the influence of thermal effects). The pressure difference between the pressure inside the bubble (containing saturated vapor at the given temperature) and the surrounding liquid represents a mechanical driving force for mass transfer. Examples of this type of cavitation model are the Schnerr–Sauer model [27], the Kunz et al. model [28], the Zwart–Gerber–Belamri model [29], and the model by Singhal et al. [30]. Within the EOS-type models, mass transfer is based on thermodynamic relations for the phase mixture, with pressure representing one of the thermodynamic properties governing the phase-change process [31]. The so-called homogeneous equilibrium model (HEM) assumes a thermal equilibrium between the liquid and vapor phase, whereas in barotropic models, density only depends on pressure, and an energy equation does not have to be considered. In contrast, the homogeneous relaxation model (HRM) determines the mass transfer rate based on the thermal nonequilibrium between the phases [31]. For a more detailed and complete list of cavitation models and their classification, the reader is referred to [32].

The presence of non-condensable gas(es) and its release/evolution from or re-adsorption/dissolution into the liquid phase affects the overall flowfield and can thereby influence flow cavitation; see, for example, [12,33] discussed below. In addition, similar to impurities on the wetted surfaces of wall-bounded flows and suspended solid particles in the flow, microscopic amounts of non-dissolved gas serve as cavitation nuclei. Increasing the amount of dissolved gases leads to an increase in the nucleation rate and results in an elevation of the liquid's vapor pressure and a reduction in its tensile strength for cavitation inception, see [34–36].

Since the gas evolution or dissolution process is diffusion-based and, therefore, slow in comparison to the phase-change process in vapor cavitation, some cavitation models limit the dynamics of the non-condensable gas (originally present in the flow in the form of nuclei or microbubbles) to its expansion or contraction based on the flowfield conditions, see [30,31,33]. Other models capture the co-existence of both vapor and gaseous phases in a single bubble, thereby being able to predict phenomena such as cavitation-induced gas release; see, for example, [21,34,37–39]. Note that an arbitrary combination of the prescribed multiphase and mass transfer models is not always possible.

For completeness, some of the above-mentioned references are briefly addressed in terms of their stated objectives.

Battistoni et al. [31] compared the results of two different simulation models for cavitating flow through a test nozzle (under full cavitation conditions) with experimental data by Duke et al. [23]. The first simulation model uses a mixture model in conjunction with a VOF formulation (as implemented in the CFD solver CONVERGE (2.1.0) [40]) together with an HRM cavitation model. The second model approach uses a multifluid Eulerian approach I in conjunction with a simplified R-P equation for calculating mass transfer due to vapor cavitation, as implemented in the solver AVL FIRE™. The model also accounts for vapor bubble coalescence and disintegration by tracking the number density and interfacial area density of vapor bubbles. The non-condensable gas phase (air), on the other hand, was assumed to be a dispersed phase of bubbles with a constant diameter of 1  $\mu\text{m}$ . In both models, the gaseous phase was assumed to be free (non-dissolved) at all times and was taken into account in the mixture density; volume or mass fraction equations were solved for all three phases (liquid, vapor, and gas).

Comparison with the experimental data showed that the multifluid Eulerian model more accurately predicts mass flow rate, total void fraction, and liquid stream reattachment to the wall than the mixture model. In a later study, Battistoni et al. [33] provided an

in-depth numerical analysis based on the prescribed mixture model for the same geometry under standard and de-gassed conditions. They demonstrated good agreement with experimental data [23] for these two test cases. However, experimental data collected later for the same test cases [25] but using a nozzle made of beryllium alloy, rendered the physical arguments arising from the numerical results questionable.

Motivated by the data presented in [25], Yang and Habchi [34] proposed a fully compressible two-phase flow model based on phase-equilibrium theory and non-linear real fluid equation of state for liquid and gas phases, whereby both phases are considered as multicomponent systems containing either vapor and free gas or liquid and dissolved gas. The authors implemented their real fluid-phase model into the flow-solver IFP-C3D [41] but with turbulence being modeled via LES and the Smagorinsky subgrid-scale model. While their simulations for the non-degassed case agreed well with experimental data, results for the degassed case were predicted to be much more fragmented in the occurrence of cavitation than found experimentally.

Assuming thermodynamic equilibrium and neglecting thermal effects, Iben et al. [37,38] conducted numerical simulations on a planar micro-nozzle using a mixture model in conjunction with a HEM cavitation model. The liquid phase was considered weakly compressible, and the vapor and released gas were compressible using suitable equations of state. Vapor mass fraction was obtained directly as a function of the prevailing fluid pressure; the evolution of dissolved gas was limited to its release into existing vapor bubbles or cavities and governed using a combination of Henry's law valid at the bubble or cavity interface and Fick's law governing the transport of dissolved gas within the liquid phase. The observed cavitation-induced gas release was similar in nature to that observed by Yang and Habchi [34].

Numerical simulations of the cavitation test geometry previously investigated by Nurick [14] and also presented as part of the present investigation have been analyzed by several authors. Singhal et al. [30] were the first to consider this case as a test case for their full cavitation model and its implementation in the commercial flow-solver CFD-ACE+. Their results for the discharge coefficient compared well with Nurick's correlation (derived from test data), even though values are consistently slightly higher than Nurick's correlation curve for the cavitating flow regime. The onset of cavitation was reported to occur at a cavitation number of 1.7, analogous to correlation data. Numerical simulations of this case based on a homogenous mixture model and considering a three-phase (liquid, vapor, and non-condensable gas) system were also carried out by Darbandi et al. [42]. They employed the full cavitation model by Singhal et al. [30], even though there are some inconsistencies in their reported formulation of the vapor condensation source term. Their results for the discharge coefficient as a function of a cavitation number agree well with the experimental measurements by Nurick and the simulation results reported by Singhal et al. [30], even though their values were consistently below those predicted by the latter authors. Both Singhal et al. [30] and Darbandi et al. [42] assumed the incoming flow to contain non-condensable gas with a mass fraction of 15 ppm dissolved in the liquid phase (i.e., water). Note that, in his experiments, Nurick [14] did not report the amount of dissolved gas contained in their water supply system. He did, however, report the aspiration of air between the test orifice and the measurement system under some conditions. Later, Darbandi et al. [43] compared their prior simulation results [42] with predictions from a mixture model for a two-fluid (liquid and vapor) system without dissolved gases and based on a cavitation model similar to that by Schnerr and Sauer [27]. They found that results for the discharge coefficient from the three-phase model agreed better with experimental results than the two-phase model results. Cavitation inception, i.e., the onset of cavitation, is found to occur at a higher cavitation number for the case with the dissolved gases considered in the model (i.e., 1.69 versus 1.51).

Nurick's nozzle geometry (made of Lucite) was also analyzed by Lifante and Frank [44] in the context of a validation effort regarding their implementation of the Zwart–Gerber–Belamri model [29] for vapor cavitation and the dissolved non-condensable gas model by

Yang et al. [45] in the commercial flow-solver ANSYS CFX. Their results for the discharge coefficient agree better with Nurick's correlation than those by Singhal et al. [30] in the cavitating regime, but underpredict its value in the non-cavitating region. As part of an investigation on cavitating aircraft ejector pumps, Mehring [12] also analyzed Nurick's Lucite nozzle geometry for both water and jet-A, both with dissolved air in the liquid phase (based on equilibrium conditions) and free air in the form of bubble nuclei in the upstream flow. Later, Coussirat et al. [46] also studied this orifice geometry using ANSYS Fluent with a focus on the effect of different turbulence models, their calibration and by employing the Zwart–Gerber–Belamri model [29] and Singhal et al. [30] model.

The model equations employed within the numerical analysis conducted as part of the present work closely relate to those employed by Lifante and Frank [44] and are presented in Appendix A. Specifically included herein are also the model equations for the dissolution and evolution of non-condensable gases, which have previously been detailed and explained only in [45]; a reference which is not readily available.

Effects of varying the amount of dissolved gas in the flow were not investigated in any of the prescribed investigations based on Nurick's nozzle geometry, even though Coussirat et al. [46] considered small amounts of dissolved gases for calibrating their model(s). To the authors' knowledge, Coussirat et al. were also the only ones to compare, aside from the predictions for the discharge coefficient, predicted local wall-pressure data with the respective data measured by Nurick. The present work rectifies these shortcomings by providing experimental data and numerical analysis for Nurick's orifice geometry under the systematic variation of the amount of dissolved gas (CO<sub>2</sub>) in the upstream flow.

## 2. Basic Definitions for Orifice Flows

The likelihood for the flow through a contracting orifice, as depicted in Figure 1, to develop cavitation can be characterized by the cavitation number,  $CN$ , which is commonly defined as:

$$CN = \left( \frac{p_1 - p_v}{p_1 - p_2} \right), \quad (1)$$

where  $p_1$  and  $p_2$  are the pressures upstream and downstream of the orifice (see Figure 1) and  $p_v$  denotes the (equilibrium) vapor pressure of the liquid.

The dimensionless cavity pressures at the position of the pressure taps shown in Figure 1 are defined as:

$$P_{cav1,2} = \frac{p_{cav1,2}}{p_1 - p_2}, \quad (2)$$

where  $p_{cav1}$  and  $p_{cav2}$  denote the dimensional wall-static pressures measured at a distance  $d/4$  and  $d/2$  downstream of the contraction (see Figure 1). The actual mass flow rate through an orifice can be characterized using the discharge coefficient, which is defined as:

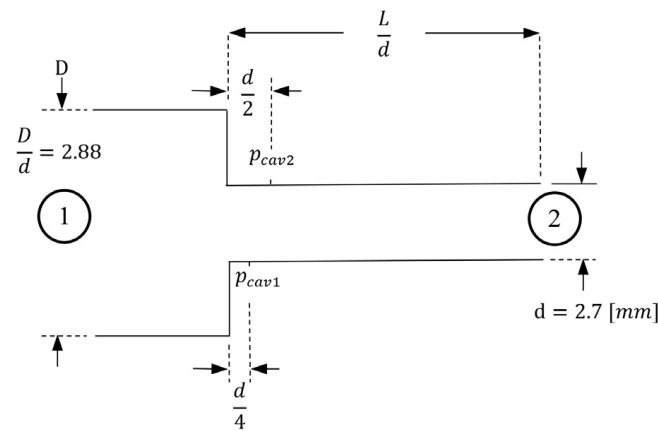
$$C_d = \frac{\dot{m}_a}{\dot{m}_t}, \quad (3)$$

where  $\dot{m}_a$  and  $\dot{m}_t$  represent the actual and the theoretical mass flow rates, respectively. The theoretical mass flow rate describes the mass flow in the absence of any losses. In our case, it can be written as the mass flow rate through a straight tube of diameter  $d$  with the same pressure conditions as for the orifice case and without any frictional losses, i.e.,

$$\dot{m}_t = \frac{\pi d^2}{4} \sqrt{2\rho_l(p_1 - p_2)}, \quad (4)$$

where  $\rho_l$  denotes the fluid density (liquid water). Various expressions can be found in the literature for determining the discharge coefficient. A vital consideration in this context is the presence or absence of cavitation in the nozzle. Since the cylindrical orifice geometry investigated here (and as shown in Figure 1) conforms to the Lucite orifice considered

by Nurick [14], except for a scale-down factor of  $(d/d_{Nurick}) = 2.7/7.6$ , we use Nurick’s analytical expressions for the cavitating flow in the nozzles as a reference.

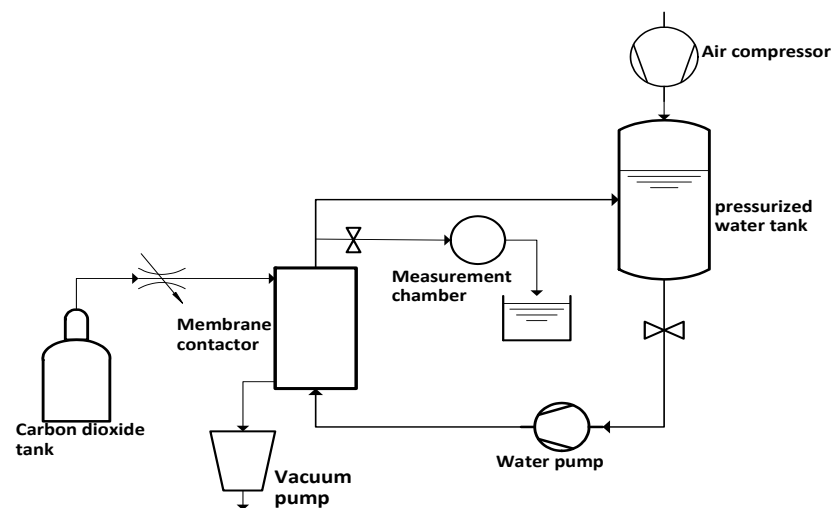


**Figure 1.** Geometry and dimensions of the investigated sharp-edge cylindrical test orifice and positions of cavity pressure taps 1 and 2 downstream of the sudden contraction. A scaled-down version of Nurick’s Lucite orifice [14].

### 3. Experimental Test Setup

#### 3.1. Water-Preparation Cycle

In order to investigate the effect of dissolved gases on cavitation inception and its evolution, the amount of non-condensable dissolved gases has to be adjustable and controllable in the experimental setup. In an upfront water-preparation cycle, water is pumped from the bottom of a tank to a membrane contactor, where the absorption and desorption of gases in or out of the liquid takes place, see Figure 2 in this context.



**Figure 2.** Schematic diagram of the water-preparation cycle in the experimental setup.

The contactor contains inlet and outlet ports for water as well as for the gas. For the degasification of water, a vacuum pump is connected to the corresponding gas port of the contactor while the “sweep” gas port remains closed. In order to dissolve non-condensable gases in water, the contactor is used in sweep mode. For this purpose, the “sweep” gas is introduced to the contactor at the corresponding gas port while the vacuum gas port remains closed. At suitable time intervals water samples are taken and guided to the measurement chamber at suitable time intervals, where the gas sensors measure the dissolved gas concentration. Dissolved oxygen is measured using an optical oxygen sensor (Orbisphere M1100 Luminescent oxygen sensor, Hach Lange GmbH, Loveland, CO,

USA), and nitrogen and carbon dioxide concentrations are measured using two thermal conductivity gas sensors (the Orbisphere 31590HP nitrogen sensor and Orbisphere 31490TC carbon dioxide sensor Hach Lange GmbH). To reach higher gas concentrations, an air compressor is utilized to increase the pressure level within the system. In this work, we use carbon dioxide as a test gas because of its higher solubility in comparison to nitrogen and oxygen. Water with five different dissolved carbon dioxide concentration levels is prepared for testing purposes. Table 1 summarizes the dissolved gas concentrations for the five investigated cases.

**Table 1.** In water, dissolved gas concentrations for the five investigated cases GC1–GC5.

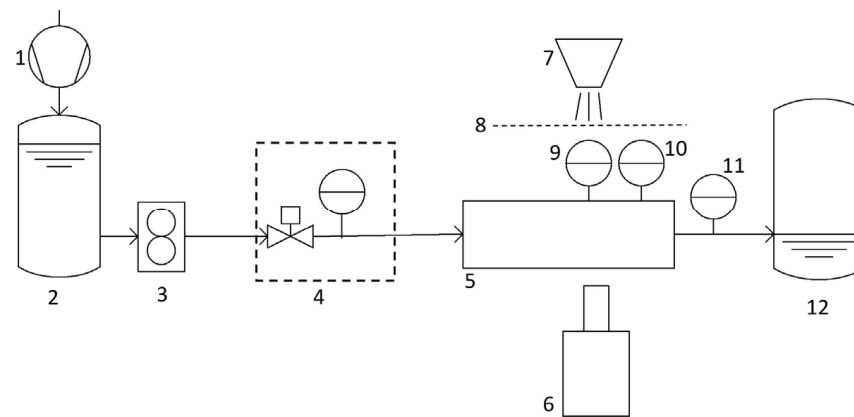
| Gas Type       | Mass Concentration [ppm] |      |      |      |      |
|----------------|--------------------------|------|------|------|------|
|                | GC1                      | GC2  | GC3  | GC4  | GC5  |
| Carbon dioxide | 0                        | 318  | 707  | 1060 | 1493 |
| Oxygen         | 0.85                     | 1.09 | 0.42 | 1.02 | 0.52 |
| Nitrogen       | 2.03                     | 2.41 | 1.30 | 2.28 | 1.67 |

### 3.2. Cavitating Orifice Flow–Flow Measurements

Cavitation inception is investigated for water flowing through the sharp-edged orifice illustrated in Figure 1. The test section (i.e., drilled and polished) was made out of PMMA for flow visualization purposes. The orifice is a scaled-down version (scale factor  $2.7/7.6 \approx 35.5\%$ ) of the Lucite orifice employed by Nurick [14]. The scale-down was necessary due to flow rate limitations based on the available water tank volume and the required testing time to assure steady-state conditions for each measurement. For cavity pressure measurements, two wall pressure taps have been precision drilled and are located at a  $d/2$  and  $d/4$  distance from the sharp-edged contraction across which the cylindrical cross-section reduces from diameter  $D$  to  $d$ . Figure 3 depicts our experimental setup for the cavitation inception measurement in an orifice flow. In the employed flow system setup, water flow is maintained by pressurizing the water tank using an air compressor, providing tank pressures of up to 10 bar. The orifice inlet pressure must be precisely regulated to resolve the inception point accurately. This has been accomplished using a back-pressure regulator. The water mass flow rate is measured upstream of the orifice using a magnetic mass flow meter (Promag P 10, 5PBB15, Endress + Hauser Group Services AG, Reinach, Basel, Switzerland.). Experiments and respective measurements were conducted for orifice inlet absolute pressures between 0.96 bar and 3.45 bar. A high-pressure build-up in the tank (10 bar) just behind the pressure valve guarantees that the orifice inlet pressure remains constant during the experiments. No free or evolved gas was observed at the orifice inlet within our experiments. Experiments were performed in batch mode; that is, data for each operating point were collected separately. Measurements of cavity pressures  $p_{cav1,2}$ , pressures  $p_{1,2}$  upstream and downstream of the orifice, and the mass flow rate  $\dot{m}_a$  were taken simultaneously for a duration of 5 s after quasi-steady flow conditions through the orifice were reached. The temporal resolution of the employed mass flow meter is 1 Hz, that of the wall pressure tap sensors 20 Hz, and for upstream and downstream pressure sensors 1 Hz. The accuracy of the latter sensors is  $\pm 0.5\%$  of the full-scale measurement range, and that of the sensors employed for the pressure taps is  $\pm 0.35\%$ . The accuracy of the mass flow meter is  $\pm 0.5\%$  of the actual measurement value.

Note that in the experiments conducted by Nurick [14], the flow (after leaving the orifice) was directly discharged into a pressure-regulated tank filled with nitrogen, allowing the study of the hydraulic flip. In contrast, in the present work, the orifice is connected to a larger diameter pipe section, allowing the flow to expand before discharging into a filled water tank. For some experiments, this pipe was made of PMMA as part of the test orifice. This allowed the observation of gas bubbles downstream as a consequence of outgassing or gas cavitation throughout the orifice flow section.



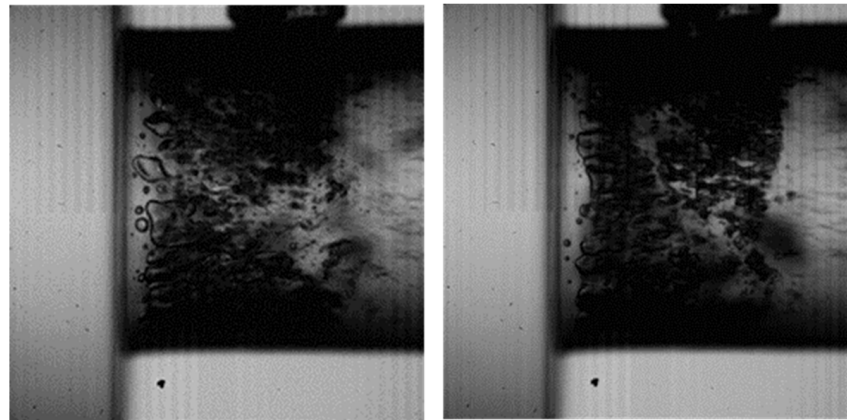


**Figure 3.** Flow-system and measurement setup for cavitation inception experiments. 1: air compressor, 2: pressurized water tank, 3: flow meter, 4: pressure regulator unit, 5: PMMA orifice, 6: high-speed camera, 7: LED light, 8: light diffuser, 9: cavity pressure sensor, 10: cavity pressure sensor, 11: downstream pressure sensor, and 12: water tank.

### 3.3. Cavitating Orifice Flow–Flow Visualization

Diffuse backlight illumination was used for flow visualization. A 50W LED chip was used as a light source and placed behind the test article. To ensure uniform illumination of the observation window and prevent any bright spots, a diffuser sheet was placed between the test article and the light source. This was necessary for imaging the orifice with a relatively large field of view (see, for example, Figures 10 and 11 below). Flow visualization for a small field of view is exemplary, shown in Figure 4, for an area just after the contraction. Here, imaging was performed without a diffuser because the light distribution on that field of view was reasonably homogenous. Images were captured using a high-speed camera (Photron FASTCAM SA-Z) equipped with a zoom system lens to achieve the desired magnification for three different sizes of the field of view (see, for example, Figure 4, Figure 10, and Figure 11). The Images in Figure 4 were captured at a frame rate of 4000 frames per second (fps) to capture more details of the bubble dynamics at the contraction. Removing the diffuser cover, in this case, was also necessary in order to reach the higher light intensity necessary for imaging at high magnification and high frame rates. Images such as those shown in Figures 10 and 11 were captured at a frame rate of 1000 fps to show the overall flow characteristics in the orifice and to observe the fluid flow over a longer time period, especially in the context of the unsteady flow at transition points (See for example Figure 10, GC5,  $CN = 1.80$ ). It is important to note that cavitation bubbles or cavitation clouds for the attached cavitation illustrated in Figure 10 appear blurry, i.e., not sharp, compared to the images in Figure 4 because the focal planes in both sets of images are different. The focal plane of the images in Figure 10 was set to coincide with the position of the pressure taps, i.e., the plane through the centerline of the orifice, allowing the observation of the flow near the walls (top and bottom region in the images) and also in the center region of the orifice. Cavitation bubbles or cavitation clouds do not appear sharp in those images because they are generated at the walls around the entire circumference, which includes out-of-focus areas between the focal plane and the camera. In Figure 4, the focal plane was adjusted so that bubbles generated in the wall near the region closest to the camera appear exactly on the focal plane, unobstructed from any other flow features. In this case, we can even see the scratches located on the inner wall surfaces of the test article. The prescribed optical interrogation technique follows the work of others; see, for example, Sou et al. [25] and Stanley et al. [47], and differs from standard shadowgraphy or Schlieren photography frequently used for investigating cavitating nozzle flow [48]. The present method solely aims to identify the overall flow structure without aiming to extract details of that structure or quantitative information such as local density. Other optical methods in the visible spectrum, which provide, for example, information about local vapor fraction or information on fluid velocity, do exist but either limit themselves to 2D orifices, a scaled-up

flow geometry, or require additional particle seeding, thereby modifying the flow behavior, especially for small-scale orifices. See also [49].

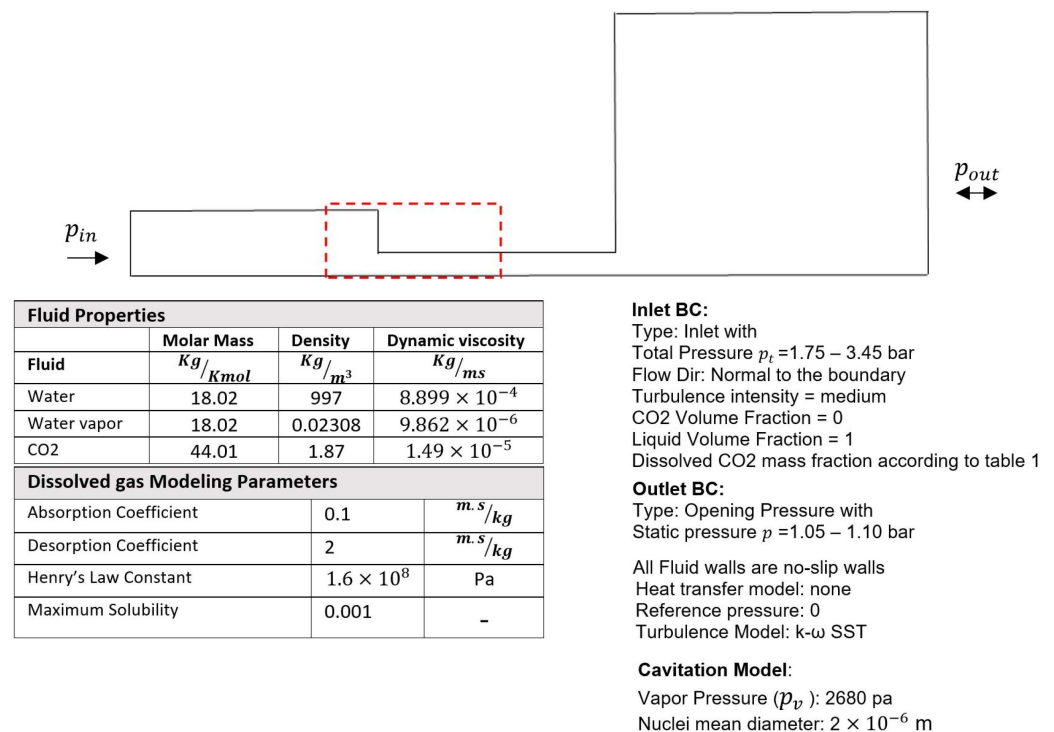


**Figure 4.** High-speed images of the flowfield just downstream of the orifice contraction show cavitation clouds at two different instances in time. The focal plane is on the orifice wall closest to the camera. Flow from right to left; backlight images without diffuser cover. Images taken with Photron FASTCAM SA-Z at a frame rate of 4000 fps.

#### 4. Numerical Analysis Model

Numerous modeling approaches have been developed to predict cavitation and outgassing phenomena in the framework of CFD simulations; see also Section 1.2 in this context. To compare our experimental results with numerical model predictions, we employ the Zwart et al. model [29] for the mass transfer between the liquid and vapor phase in combination with the outgassing model by Yang et al. [45], the latter of which is also employed in the so-called “full cavitation model” by Singhal [30]. The model employed here and the slightly different “full cavitation model” are still in widespread use in the industry today (see, for example, Mehring [12]), which motivated the use of one of these models in the present investigation. The model considers a three-phase mixture consisting of a gaseous phase of non-condensable gas, water vapor, and liquid water, which itself is considered a two-component liquid composed of pure water and dissolved carbon dioxide. The homogenous mixture assumption is employed, and all phases share the same velocity and pressure field. Here, we make use of the commercial flow-solver CFX v19.1 by ANSYS Inc., in which the prescribed models are available: see also Lifante and Frank [44] in this context. For a detailed explanation of the phase change models, the reader is referred to Zwart et al. [29], Yang et al. [45], and Lifante and Frank [44]. Values for model parameters were chosen identical to those in [44] for the same flow configuration (see Section 1.2). The  $k-\omega$  SST turbulence model [50] with standard model coefficients was used for turbulence closure. The overall governing equations solved as part of the present investigation are provided in Appendix A. Only carbon dioxide is considered a dissolved non-condensable gas for simulating the orifice flow. The mass fraction of dissolved  $\text{CO}_2$  at the inlet boundary was specified according to the experimentally investigated test cases summarized in Table 1. Analyses were only carried out for cases GC1 through GC3 due to (known) convergence issues of the outgassing model for mass fractions beyond 1000 ppm. The Henry constant for carbon dioxide was chosen from the literature to be  $H_v^{px} = 1.6 * 10^8 \left[ \text{Pa} \frac{\text{mol}_{\text{water}}}{\text{mol}_{\text{co2}}} \right]$ . The vapor volume fraction and free non-condensable gas volume fraction were both set to zero at the inlet boundary, while the nuclei volume fraction was set to 0.01247 with a nuclei radius of 2  $\mu\text{m}$ . Liquid or water vapor pressure was set to 2680 [Pa]. Figure 5 provides a summary of all employed model parameters and boundary conditions. For the simulations, a sharp-edge orifice was assumed. To model the 2D axisymmetric problem within the 3D CFX solver environment, a narrow one-degree wedge of the configuration with symmetry conditions in a circumferential direction was considered. Only a single computational cell

was used in that direction. In CFX, hydrodynamic equations (for velocity and pressure) and other transport equations are solved via a pressure-based coupled solver and based on an element-based finite-volume approach with a co-located (non-staggered) grid and an interpolation for pressure and velocity via FE shape functions. Steady-state solutions for the prescribed problem have been produced via pseudo-transient time-stepping with a special high-resolution upwind-type scheme for the advection terms. The solution of the linearized system of equations is obtained via an algebraic multigrid (AMG) solver. A block-structured rectilinear mesh consisting of five blocks was used in the (r-z) plane. The mesh count for the inflow and contracted flow section (three blocks) was 20,000, and the downstream expanded flow section was 21,000 (two blocks). The respective local mesh resolution is greater than that employed by Lifante and Frank [44] and Singhal et al. [30] for a similar flow configuration. Further mesh refinement did not provide any meaningful changes (<1%) in the flow properties of interest. Numerical solutions for the various cases will be presented and compared to experimental results in Section 5.2.



**Figure 5.** Summary of all employed model parameters and boundary conditions for the simulations. The dashed line illustrates the flow area displayed in Figure 14 below.

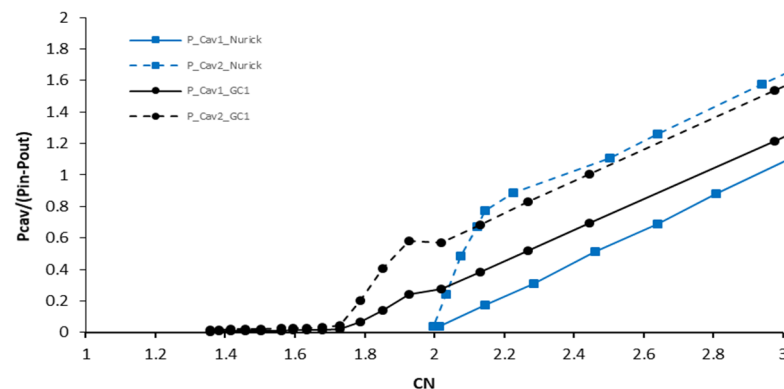
## 5. Results

### 5.1. Experimental Results

#### 5.1.1. Comparison of Measured Cavity Pressures with Results from Nurick Experiments

Figure 6 illustrates the dimensionless cavity pressures measured at tap positions 1 and 2 (as specified in Figure 1) dependent on the cavitation number  $CN$  for water with an aeration level GC1 (i.e., no dissolved  $CO_2$ ). Also shown are the results reported by Nurick for the similar (scaled-up) orifice made of Lucite [14]. Note that the latter study did not measure or report the amount of dissolved gas contained in the water supply system. Cavitation onset in the present case is found to occur at  $CN = 2.02$  and coincides with a plateau in the pressure measured at tap position 2. Full cavitation is found to occur at cavitation numbers below  $CN = 1.73$  when both pressure tap measurements are identical. The prescribed observation in regards to cavitation onset has also been made by Nurick in his original paper [14] and later again in the “Authors’ Closure” comment contained in the commentary by Peterson [51]. However, in Nurick’s experiment, the cavity pressure

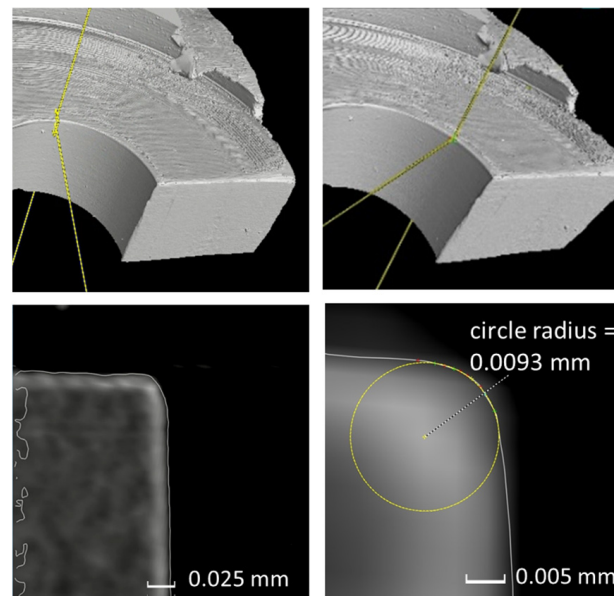
reaches the vapor pressure at a higher cavitation number, i.e.,  $CN = 2.5$ , and the plateau formation reported by Nurick is less pronounced; see Figure 6.



**Figure 6.** Comparison of dimensionless cavity pressures  $P_{cav1,2}$  at tap positions 1 and 2 (according to Figure 1), with results presented by Nurick [14] (Figure 5).

Deviations from Nurick results might be due to scale differences and differences in entrance roundness  $r$  in relation to the orifice diameter(s). As already reported by Nurick, the roundness of the sharp-edged entrance region has a significant influence on cavity pressure and, consequently, on cavitation inception [14]. In addition to entrance roundness, imperfections along the edge of the contraction caused by drilling and polishing can affect the flow through the contraction and, consequently, cavity pressures as well. These effects are expected to have a stronger impact on the cavity pressure at tap 1, which is located closer to the contraction. As noted earlier, our orifice geometry is approximately a factor 3 smaller than Nurick's Lucite orifice. However, the corner radius of our test article was indeed quite small as well. Differences in the amount of dissolved air in both cases will also impact cavitation onset, as will be discussed in detail later in the context of dissolved carbon dioxide. Assuming equilibrium conditions in Nurick's experiment, Henry's law yields a dissolved air mass fraction of 15 ppm, whereas in Case GC1, it is approximately 3 ppm (see Table 1). An explanation for the variation of pressure at the two pressure taps, including the prescribed plateau formation, at tap position 2 was already given by Nurick [14]. As the cavitation number is decreased, i.e., by increasing the upstream pressure, the pressure at both taps initially drops linearly, with the pressure at tap 2 being higher, as the latter is located in the recompression zone. It is interesting to note that Nurick explains the plateau formation in the pressure for Tap 2 as being the result of a variation of the reattachment phenomenon with cavitation onset. However, in the present investigation, the pressure curve for tap 1 also exhibits the plateau phenomena to an extent similar to that observed by Nurick [14] for the pressure at tap 2 only. This suggests that cavitation onset also changes the flow dynamics around the vena contracta, thereby initially delaying a further drop in pressure, also at tap 1. A possible explanation might be an initial decrease in shear stress in the shear layer between the flow recirculation zone next to the wall and the main flow since cavitation inception and initial vapor formation is found to occur in that shear layer; see, for example, [52]. See also Figure 14 below in this context.

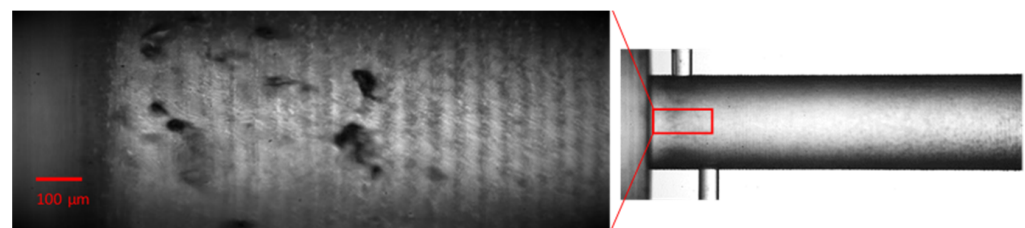
Figure 7 shows the post-test CT scans of our test orifice. The test article was cut in order to allow a better resolution for measuring the corner radius of the orifice. The measured mean corner radius was  $r = 9 \mu\text{m}$ , i.e.,  $r/d = 0.003$ . The CT scans also reveal some local topological non-uniformities along and near the edge. In the context of quantitative differences to Nurick's data observed in Figure 6, we note that aside from the prescribed geometric scale differences, there are other scaling effects that need to be considered to ensure similarity between hydrodynamically cavitating flows [53], which might have contributed to the observed differences between the present results and those reported by Nurick [14].



**Figure 7.** Top: Post-test CT scan of the orifice section with some topological anomalies along or near the edge. Bottom: Zoom-in (with different magnifications) on two edge locations identified via the yellow crosshairs in the top pictures.

#### 5.1.2. Influence of Dissolved Gas on Cavitation Inception

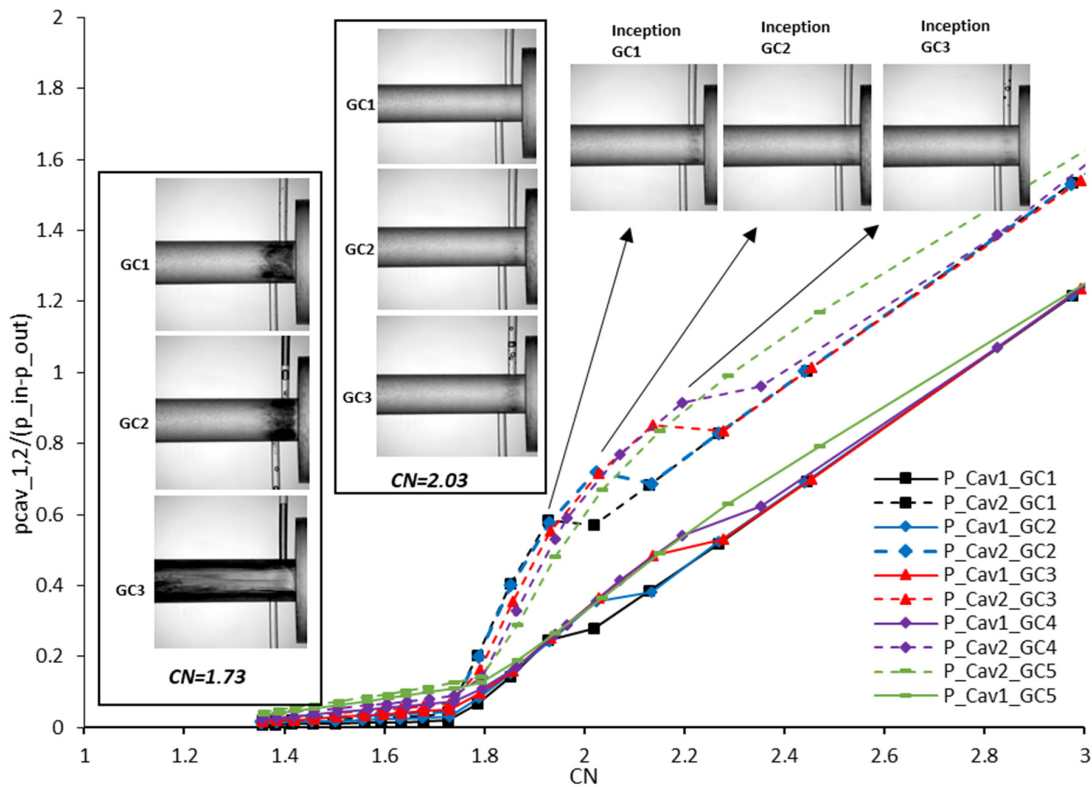
In the work presented by Nurick [14], cavitation inception was characterized by the formation of a fuzzy region just downstream of the contraction. Within the present study, flow visualization at inception using a high-speed camera (Photron FASTCAM SA-Z) shows that the observed fuzzy region consists of tiny vapor bubbles that disappear further downstream due to pressure recovery. Figure 8 illustrates the first appearance of vapor bubbles at the inception point for case GC1. The images were captured at a frame rate of 100 k [fps].



**Figure 8.** Right: Fuzzy region just downstream of the sharp-edge orifice at cavitation inception (flow from left to right). Left: Magnified view of cavitation onset indicating the presence of single cavitation bubbles (and striped structures from machining grooves on orifice walls).

Figure 9 depicts the measured change in pressures  $p_{cav1,2}$  at pressure taps 1 and 2 as a function of the cavitation number for all five  $\text{CO}_2$  aeration levels (i.e., GC1 through GC5) listed in Table 1. Each data point in Figure 9 was determined based on the time averages of cavity pressures  $p_{cav1,2}$  and upstream/downstream pressures  $p_{1,2}$  recorded during the test time of 5 s. As already noted in the previous section, the instance of cavitation inception is readily recognized by a plateau in the plot for cavity pressure  $p_{cav1}$  at tap 1. This plateau is less pronounced with increasing dissolved  $\text{CO}_2$  content; in fact, for the highest aeration level (case GC5), a plateau in the pressure curve is no longer observed. We also note that for cases GC1 through GC4, a less pronounced pressure plateau at the onset of cavitation is observed for the cavity pressure at tap 2, i.e.,  $p_{cav2}$ , as already discussed earlier in the context of Figure 6. Again, such behavior was not reported by Nurick [14]. Cavitation numbers at cavitation inception are 1.93, 2.02, and 2.14 for aeration levels GC1, GC2, and

GC3, respectively. Visual observations of inception (via the appearance of the prescribed fuzzy region) confirm these values; see the photographic inserts in Figure 9 as well as Figure 10. It can be deduced that an increase in dissolved gas concentration leads to higher cavitation numbers at inception. For fully cavitating flow, characterized here by a cavitation or multiphase cloud that extends over the entire length of the orifice, pressure values at both taps are nearly the same and always higher for higher aeration levels. See Figure 10 for  $CN < 1.73$ .




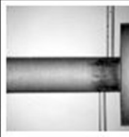
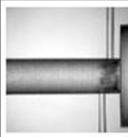
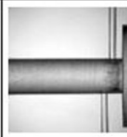
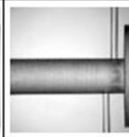
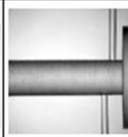
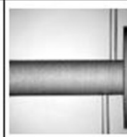
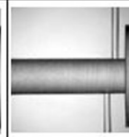
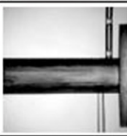
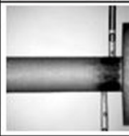
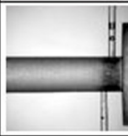
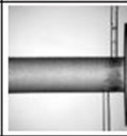
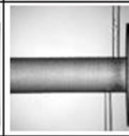
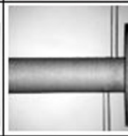
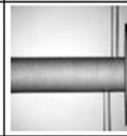
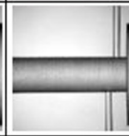
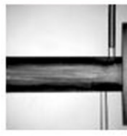
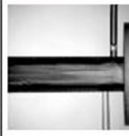
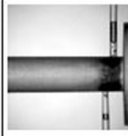
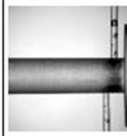
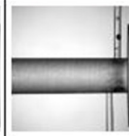
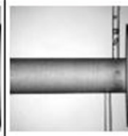
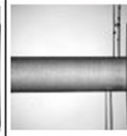
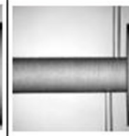


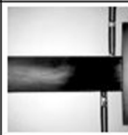
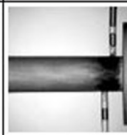
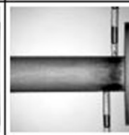
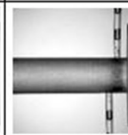
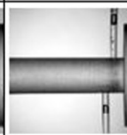
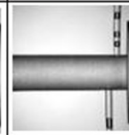
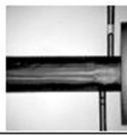
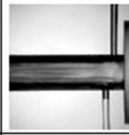
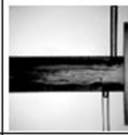
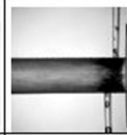
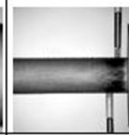
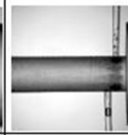
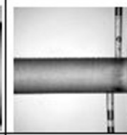
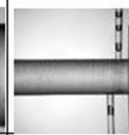
**Figure 9.** Cavitation inception and evolution as a function of dissolved CO<sub>2</sub> content. Shown are normalized pressure values at tap positions 1 and 2 (see Figure 1) as a function of cavitation number. An increase in dissolved gas concentration leads to cavitation onset at higher cavitation numbers. Accuracy <math>\pm 0.35\%</math> FSO according to IEC 60770 [54]. Flow direction in the images from right to left.

We now consider the flow images at cavitation number  $CN = 2.03$  inserted in Figure 9; for aeration level GC1, i.e., no CO<sub>2</sub> dissolved, and no cavitation occurs. This is in agreement with the information from the cavity pressure curves, according to which inception, in this case, occurs at  $CN = 1.94$ . Note that the size of the cavitation cloud for aeration level GC3 is bigger than that for aeration level GC2 at that same cavitation number, even though the cavity pressures do not vary. This indicates that the potential of cavitation generation improves with an increase in dissolved gas concentration. The effect of dissolved gas concentration on vapor cavitation is twofold: increasing the amount of dissolved gases (1) aids in the formation of cavitation nuclei and (2) increases the vapor/saturation pressure and reduces the tensile strength of the liquid [34–37]. From the images, we also note that, for case GC3, there is a notably higher amount of CO<sub>2</sub> gas bubbles being released into the access port of pressure tap 1 than in the GC2 case. In the present investigation, outgassing occurs parallel to vapor cavitation. Depending on the dissolved gas content, more or less gaseous microbubbles are being released in the flow, indicated by a slight darkening of the flow region downstream of the contraction. This is not readily seen in the photographs of Figure 10 but can be observed in the figure of Appendix B, e.g., for GC2 and  $CN = 1.86$  in comparison to GC5 and  $CN = 1.98$ . Clear evidence of these bubbles is found in the expansion section (with the exception of case GC1, due to its

very little dissolved gas content). See Figures 11 and 12 in this context. The onset of outgassing or gas cavitation is governed by the threshold or equilibrium pressure given by the sum of the liquid's vapor pressure and ( $\text{CO}_2$ ) gas-phase partial pressure, the latter being determined (under equilibrium conditions) by Henry's law [55] and the amount of dissolved gas ( $\text{CO}_2$ ) molar fraction in the liquid. In contrast, vapor cavitation occurs if the local fluid pressure drops below the critical pressure given by the sum of liquid vapor pressure augmented by the maximum principal component of the strain-rate tensor [53], including the effects of turbulent fluctuations. As water containing noticeable amounts of dissolved (non-condensable) gases passes through the flow contraction, the static pressure drops below the prescribed equilibrium pressure, leading to gas desorption. At the same time, vapor bubbles appearing in the low-pressure zone due to cavitation will collapse as soon as they migrate to areas where the fluid pressure has recovered. In contrast to vapor bubbles, gas bubble formation and dissolution occur via diffusion. Once formed, gas bubbles will persist due to the large characteristic time scale associated with this process compared to the other relevant processes. Accordingly, gas bubbles will predominantly be found well downstream of the contraction zone or in the recirculation region next to the vena contracta. Evidence of the latter is given via the gas bubbles detected in the pressure tap access ports, especially at high-dissolved  $\text{CO}_2$  concentrations. Evidence of the former is given by observations of the downstream flow for a PMMA test article, which features a transparent, extended outlet section; see Figures 11 and 12. A similar observation can also be made for aeration with air, as illustrated in Figures 17–19 of Section 5.2 in the context of a comparison to numerical analysis results.

Figure 10 summarizes the visual observations from our test campaign for all investigated  $\text{CO}_2$  aeration levels. Here, we observe again that cavitation inception shifts to higher cavitation numbers as the amount of dissolved carbon dioxide increases. Comparing fluid images for cavitation number  $CN = 1.93$ , we observe that the size of the cavitation cloud generated after the contraction is bigger or more prominent for GC2 versus GC1 (without increasing its axial length), while no free gas can be observed in the pressure ports in either case. Accordingly, while the gas content furthers cavitation, it has not yet produced considerable amounts of free carbon dioxide. Also, the cloud vanishes even before reaching the position of the second pressure tap, which demonstrates that it mainly consists of water vapor, which disappears as the static pressure in the flow recovers. By further increasing the gas content, significant amounts of gas evolve from the liquid phase, the extent of the cavitation cloud increases, and free gas is observed in the pressure ports; see Figure 10 for GC3 through GC5 at  $CN = 1.93$  or 1.94. Note that the axial extent of the cavitation cloud or multiphase region/zone has been noted in Figure 10 below each photograph. The length was determined as the time-mean value of the maximum zone length determined using high-speed videography and after suitable image post-processing (i.e., increasing image brightness and saturation, rendering the entire image white except for the wall-near the cavitation zone). Time-mean values were determined based on an imaging frame rate of 1000 fps for the entire test duration of 5 s with an image resolution of  $1024 \times 1024$  at a pixel size of  $10 \mu\text{m}$ . Also, to determine the maximum zone length in a single image, a reference flow image without cavitation was used and subtracted from the image to be evaluated. A quantification of how far vapor cavitation influences the gas evolution rate (as described by Kowalski et al. [22]) was not possible within the present study.

Figure 10 also shows that, depending on the dissolved gas concentration, the length of the cavitation zone increases with a decreasing cavitation number up to a length of about 1.1–1.6 times the orifice diameter. With a further decrease in the cavitation number, the cavitation zone suddenly expands over the entire length of the orifice and up to the downstream expansion zone; a transition occurs from cloud or bubble cavitation to extended-sheet cavitation or full cavitation, as discussed in the context of Figure 12 below.

|                                |   |   |   |   |   |  |   |   |
|--------------------------------|---|---|---|---|---|--|---|---|
| Cavitation Number, CN          | 1.68  | 1.73  | 1.79  | 1.85  | 1.93  | 2.02   | 2.13  | 2.27  |
| GC1                            |    |    |    |    |    |    |    |    |
| length of cavitation zone [mm] | Transition to full cavitation   | 3.00  | 1.95  | 1.55  | 1.31  | 0  | 0   | 0   |
| Cavitation Number, CN          | 1.68  | 1.73  | 1.79  | 1.85  | 1.93  | 2.02   | 2.13  | 2.27  |
| GC2                            |    |    |    |    |    |    |    |    |
| length of cavitation zone [mm] | Transition to full cavitation   | 3.42  | 2.48  | 2.13  | 1.72  | 1.23   | 0   | 0   |
| Cavitation Number, CN          | 1.68  | 1.73  | 1.79  | 1.86  | 1.93  | 2.03   | 2.14  | 2.28  |
| GC3                            |   |   |   |   |   |   |   |   |
| length of cavitation zone [mm] | Full cavitation   | Transition to full cavitation   | 3.41  | 2.53  | 1.97  | 1.57   | 1.26  | 0   |
| Cavitation Number, CN          | 1.69  | 1.74  | 1.80  | 1.86  | 1.94  | 1.96   | 2.07  | 2.20  |
| GC4                            |  |  |  |  |  |  |  |  |
| length of cavitation zone [mm] | Full cavitation   | Full cavitation   | Transition to full cavitation   | 4.20  | 3.43  | 2.41   | 1.72  | 1.35  |
| Cavitation Number, CN          | 1.69  | 1.74  | 1.80  | 1.87  | 1.94  | 2.04   | 2.15  | 2.29  |
| GC5                            |  |  |  |  |  |  |  |  |
| length of cavitation zone [mm] | Full cavitation   | Full cavitation   | Transition to full cavitation   | 4.70  | 4.15  | 3.61   | 2.08  | 1.40  |

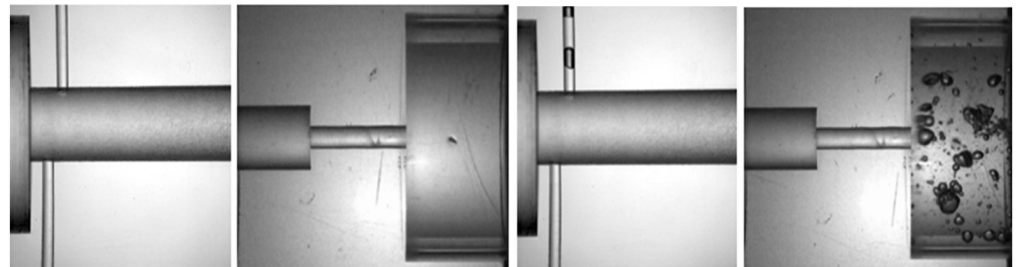
**Figure 10.** Summary of flow observations for broad range of cavitation numbers CN and 5 different mass fractions of dissolved CO<sub>2</sub>, i.e., GC1–GC5 according to Table 1. Presence of dissolved CO<sub>2</sub> accelerates cavitation development. Accumulation of evolved gas in pressure ports with decreasing cavitation number indicates that outgassing, i.e., gas cavitation, occurs parallel to vapor cavitation. Transition from confined cloud/bubble cavitation to extended-sheet cavitation, i.e., fully cavitating flow, is also influenced by dissolved gas content. Flow direction from right to left.



In the cloud or bubble cavitation stage, the cavitation zone is filled with highly dispersed vapor or vapor/gas bubbles influenced in part by the dynamics of the downstream flow reattachment and re-entrant jet dynamics. The zone appears dark in the photographs due to excessive light scattering at the many phase interfaces in the annular flow section occupied by vapor/gas bubbles. At the fully cavitating stage, core flow re-attachment does not take place. A continuous cavitation sheet filled with vapor and gas extends from the contraction throughout the entire length of the orifice. In this case, light is merely scattered at the orifice walls and the surface of the continuous annular gas/vapor cavity surrounding the liquid core flow region.

For cases with high dissolved gas concentrations and prior to cavitation onset, enough  $\text{CO}_2$  evolves in the recirculation zone around the vena contracta, such that it can be observed in the pressure tap connection channels; see Figure 10 for cases GC4 and GC5 at  $CN = 2.2$  and 2.29, respectively. In Appendix B, we include a second set of experimental data from our test campaign for similar conditions as presented in Figure 10 but with a frame of view more focused on the flow area after the contraction. This set of figures also supports the prescribed observations and illustrates the repeatability of our results.

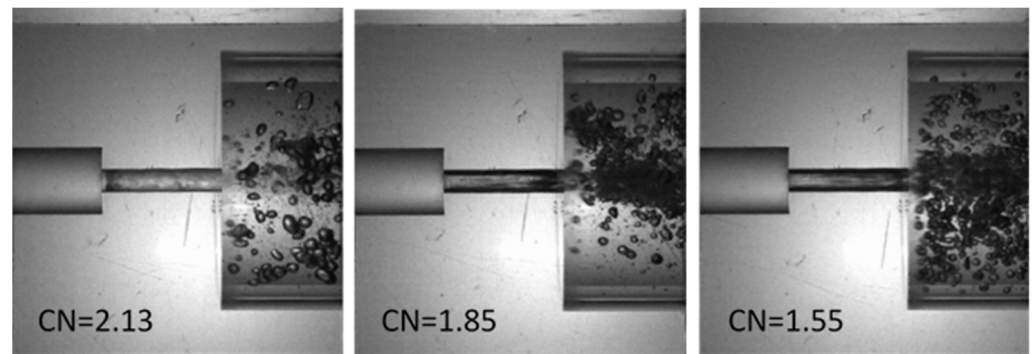
To readily observe the outgassing process ahead of the onset of vapor cavitation and to illustrate the entire flowfield under sheet- or full-cavitation conditions, a test article was produced without pressure tabs and with both the orifice and the downstream expanded outlet section made of PMMA, i.e., acrylic glass. Figure 11 illustrates results obtained for both test articles under non-cavitating conditions (cavitation number  $CN = 2.5$ ) for two specific cases: (1) with little or no dissolved gas (corresponding to case GC1) and (2) with a large amount of dissolved  $\text{CO}_2$  (corresponding to Case GC5) in the upstream flow. For the “degassed” case, no bubbles or microbubbles are visible within the entire flow domain. In contrast, for the highly aerated case,  $\text{CO}_2$  microbubbles grow, potentially coalesce, and become observable in areas where their flow residence time has become large enough, i.e., in the pressure port(s) connected to the flow recirculation zone and the downstream expanded outlet section.



**Figure 11.** Visualization of  $\text{CO}_2$  outgassing for non-cavitating flow at  $CN = 2.5$  for a test article with pressure ports and a test article w/o pressure ports but with a transparent, extended outlet section. Left: degassed water, right: highly aerated water. Accumulation of evolved  $\text{CO}_2$  gas in the access port of pressure tap 2 shows that outgassing occurs near the contraction or vena contracta in the form of microbubbles expanding in zones with slow flow velocity, including the extended outlet zone. Flow direction from left to right.

Figure 12 visualizes the evolution of the multiphase flow in the orifice and the extended outlet zone for highly aerated water (dissolved  $\text{CO}_2$  concentration similar to case GC5) with changes in the cavitation number, i.e., from  $CN = 2.13$  (early cavitation),  $CN = 1.85$  (transition to full cavitation),  $CN = 1.55$  (full/sheet cavitation). At  $CN = 2.13$ , a small cavitation region establishes after the contraction indicated by the darkened area. After the pressure recovers, the downstream orifice retains a darkened color, indicative of the formation of gaseous microbubbles. The patchy appearance might be indicative of non-uniform bubble growth and/or nuclei distribution associated with the flow dynamics in the cavitation region; it might also be related to the complexity of the turbulent flow with microbubble accumulation correlating to turbulent flow structures. At  $CN = 1.85$ , a

continuous gas/vapor annular core has formed almost along the entire length of the orifice, characterized by a smoother streaky appearance; the extended darkened region prior to the flow expansion into the downstream section is indicative of flow reattachment and re-entrant jet dynamics. At  $CN = 1.55$ , the flow reattachment zone has reached the downstream edge of the orifice, although the gas/vapor annulus does not extend meaningfully into the expansion section. With continuous operation, more and larger bubbles start to form in the recirculation region surrounding the free jet in the downstream expanded flow section.



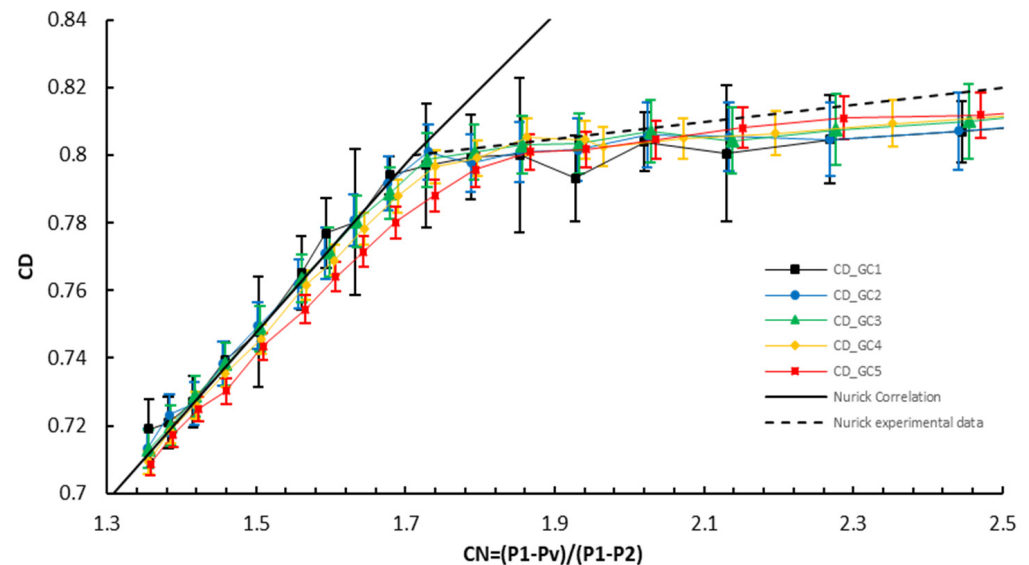
**Figure 12.** Cavitation development for highly aerated water with a reduction in cavitation number. Due to high amounts of dissolved carbon dioxide, outgassing occurs at higher rates. At cavitation number  $CN = 1.85$ , we observe full cavitation. Flow direction from left to right.

### 5.1.3. Measurements of the Discharge Coefficient

Figure 13 shows a comparison of the orifice discharge coefficients  $C_d$  calculated according to the equations presented in Section 2 and based on the present experimental results for the five investigated  $CO_2$  aeration levels (see Table 1). Each data point in Figure 13 was determined based on the time averages of upstream/downstream pressures  $p_{1,2}$  and mass flow rates recorded during the test time of 5 s. Also shown is the correlation presented by Nurick for this orifice geometry [14] without considering dissolved gas content (thick solid black line) together with a linear approximation of the experimental data reported by the same author at higher cavitation numbers under different back-pressure conditions (thick dashed black line). See Figure 8 in [14] for  $L/d = 6$ .

We note that for low-dissolved  $CO_2$  content, discharge coefficients from the current measurements agree reasonably well with those presented by Nurick, although measurement uncertainties for the lowest dissolved gas content (GC1) were considerable. Also, even though the amount of dissolved  $CO_2$  changes the cavitation number  $CN$  at which cavitation first occurs (see the discussion in the prior section), it does not notably change the variation of discharge coefficient  $C_d$  with  $CN$  for lower aeration levels, i.e., cases GC1 and GC2. At higher dissolved gas content (i.e., for cases GC3–GC5), gas evolution, i.e., gas cavitation, is increased at the same  $CN$  number, which might also significantly enhance vapor cavitation (possibly also vice versa) (see Figure 10) and the evolved gas volume fraction leads to further blockage of the flow cross-section, thereby leading to a notable drop in the discharge coefficient; see Figure 13. Despite variations in some of the instantaneously measured values, illustrated by the error bars in Figure 13, the measured average mass flow rates at a given cavitation number clearly decrease as the amount of dissolved carbon dioxide increases. Note that variations in instantaneous mass flow measurements were smallest for the cases with larger dissolved gas contents, i.e., GC3–GC5. The prescribed differences in mass flow rates for different dissolved gas content continuously decrease once the cavitation number drops below the value where full cavitation (as discussed earlier) occurs in all cases, i.e., below  $CN = 1.73$ . As the cavitation number continues to decrease below this value, the vapor-to-gas volume fraction continuously increases, diminishing the effect of the evolved gas on mass flow rate, as well as the pressure conditions at the two pressure taps. Below  $CN = 1.35$ , the discharge coefficient and pressure values at the two

pressure taps become independent of the amount of dissolved gas originally contained in the liquid.

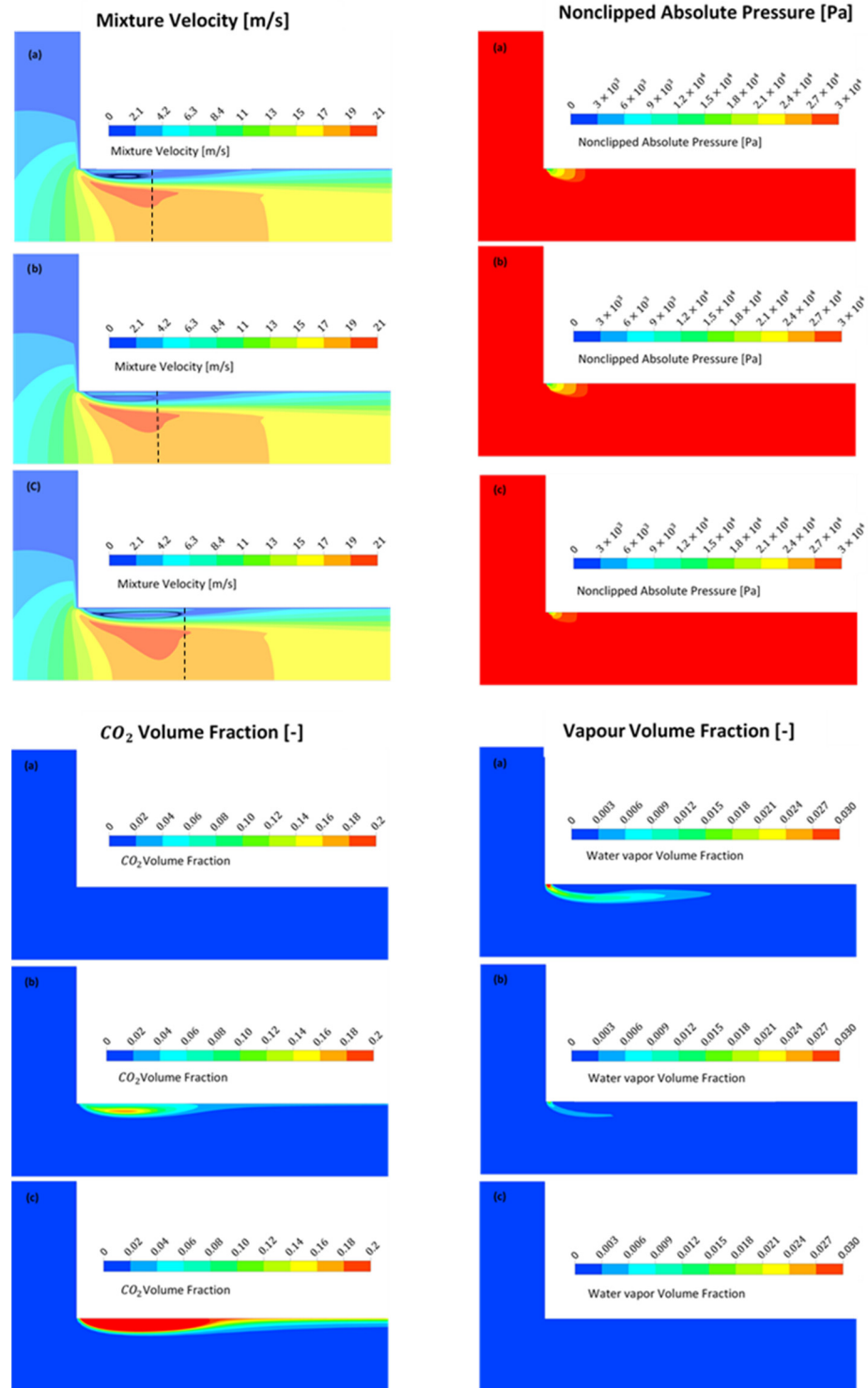


**Figure 13.** Discharge coefficient  $C_d$  as a function of cavitation number  $CN$  and dissolved  $\text{CO}_2$  gas content (GC1–GC5 according to Table 1) together with data from Nurick [14]. Increasing gas content leads to a decrease in the discharge coefficient, especially near the onset of full cavitation. Here, evolved gas contributes meaningfully to liquid phase displacement resulting in lower mass flow rates.

## 5.2. Numerical Analysis Results

Figure 14 illustrates simulation results based on the numerical analysis model described in Section 4 for the three experimentally investigated dissolved gas configurations GC1, GC2, and GC3 at cavitation number  $CN = 1.85$ . (As mentioned already in Section 4, convergence issues with the outgassing model for high mass fractions prevented the analysis of cases GC4 and GC5.)

One observes that the velocity fields for the three cases do not differ significantly, even though the predicted minimum absolute pressure found near the wall just after the contraction is larger if the dissolved gas concentration of the upstream flow is larger. Correspondingly, the size of the low-pressure zone is predicted to decrease with increasing dissolved gas concentration. As a result, we observe less cavitation (a lower vapor production rate) with increased dissolved gas concentration. In fact, for the highest dissolved gas content (case G3), the flow is not cavitating at all. The numerical results suggest that cavitation inception occurs at lower cavitation numbers for higher dissolved gas content. This is in contrast to our experimental observations (see the discussion in Section 5.1.2) and will be further addressed later on.



**Figure 14.** Contours of predicted absolute velocity (top, left), absolute pressure (top, right), gaseous CO<sub>2</sub> volume fraction (bottom, left) and water vapor volume fraction (bottom, right) near the sharp-edged contraction for  $CN = 1.88$  and different values for dissolved-gas content in the upstream flow, i.e., (a–c) corresponding to G1, G2, and G3 according to Table 1. The axial length of the recirculation zone measured from the contraction is 1.35 mm (a), 1.47 mm (b), and 1.94 mm (c), as indicated by dash marks in the velocity contour plots. The area experiencing cavitation shrinks with an increase in gas content. Cavitation occurs in the shear layer between the flow recirculation zone and the core flow; evolved CO<sub>2</sub> remains highest in the flow recirculation zone and, for high dissolved CO<sub>2</sub> concentrations in the near wall region further downstream. Flow direction from left to right.

The results presented in Figure 14 also show that with increasing dissolved CO<sub>2</sub> concentration in the upstream flow, the amount of gaseous CO<sub>2</sub> released out of a solution near or around the vena contracta increases and accumulates in the recirculation zone. Experimental evidence for this gas release is given by gas bubbles in the pressure ports at these operating conditions, as shown in Figure 10. Taking the dividing streamline between core flow and recirculation zone as a reference, the simulations show that with increasing the dissolved gas content from GC1 to GC3, the depth of the recirculation zone at the positions of pressure taps 1 and 2 increases by about 10% and 15%, respectively. For case GC3, its depth at Tap 2 is about 10% of the orifice diameter. To distinguish between the onset of outgassing versus the onset of cavitation, we observe Henry's constant discussed in Section 4 and the resulting equilibrium pressure based on Henry's law. Because the local equilibrium pressure of the dissolved CO<sub>2</sub> is higher than the water vapor pressure, the onset of CO<sub>2</sub> outgassing occurs prior to fluid cavitation. The reader is referred to Figures 9 and 11 in this context.

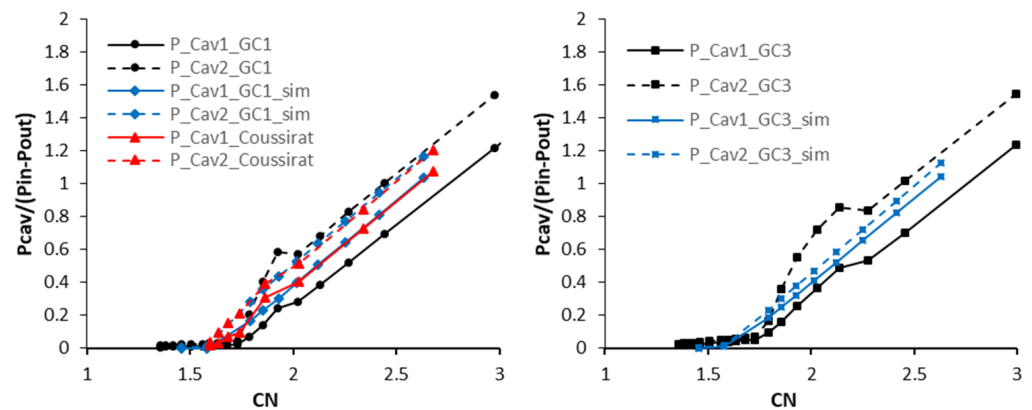
Figure 11 visualizes flow characteristics in the orifice and the extended outlet section of the test setup for degassed and highly aerated water at cavitation number  $CN = 2.5$ . As illustrated in Figure 9, no fluid cavitation occurs at this cavitation number, and no fuzzy region can be found near the contraction. However, gas bubbles can be observed in the extended outlet section in Figure 11 and also in the pressure port at tap 2 in Figure 9 for this case, which is indicative of gas release.

Despite the prescribed differences, computed mass flow rates through the orifice for the three cases GC1–GC3 at the investigated cavitation number ( $CN = 1.85$ ) differ by less than 0.5%. The mass flow rate predicted for case GC3 is  $\dot{m} = 0.0735$  kg/s and only 2% above the experimentally measured value. The discharge coefficient calculated from the measured data for this case is  $C_d = 0.792$ . This value is slightly below the experimental data reported by Nurick at the same cavitation number (see Figure 13).

Figure 15 illustrates computed results for non-dimensional wall-static pressures at the location of pressure tap 1 and 2 (denoted by subscripts "Cav1" and "Cav2") as a function of the cavitation number  $CN$  for cases GC1 and GC3, whereby the former case corresponds to no dissolved CO<sub>2</sub> (see Table 1). Computed results for case GC2 have been excluded here since they compare closely to those for case GC1. Cavitation onset is predicted to occur at  $CN = 1.85$  for case GC1 and at  $CN = 1.79$  for GC3, respectively. Also included in the diagrams are experimentally measured values, as already presented in Figure 9, with the plateau formation indicative of cavitation onset.

An initial increase in the amount of dissolved CO<sub>2</sub> (i.e., from GC1 to GC2) does not have a noticeable effect on computed cavity pressures at tap 1 and tap 2. However, a higher amount of dissolved CO<sub>2</sub> (case GC3) leads to slightly higher pressures at the position of pressure tap 1 and a reduction in pressure at tap 2. The predicted rate in pressure change at taps 1 and 2 with changes in the cavitation number is in good agreement with experimental data in the non-cavitating range; however, absolute pressure values at the upstream tap (tap 1) are overpredicted. The experimentally observed formation of a pressure plateau at the cavitation onset is not captured by the numerical results. The numerically predicted pressure variations illustrated in Figure 15 provide no indication of the onset of cavitation. More importantly, cavitation onset is found to occur at lower cavitation numbers than observed experimentally, i.e., for case CG1 at  $CN = 1.85$ , whereas  $CN = 2$  in the experimental results and for case CG3 at  $CN = 1.79$ , whereas  $CN = 2.28$  experimentally. This demonstrates that the employed physical-numerical model does not properly predict the effect of the dissolved CO<sub>2</sub> gas content; i.e., while in the experiment, the onset of cavitation is moved to higher cavitation numbers with an increase in dissolved gas content, the numerical results predict the cavitation onset to occur at lower cavitation numbers with an increase in dissolved gas content. From the discussion on numerical studies of cavitating orifice flows and dissolved gas effects (see Section 1.2) and the various existing modeling approaches, it is clear that the currently employed analysis model(s) have considerable limitations, leading to the prescribed differences between numerical and

experimental results. These limitations include: (1) no slip between the phases based on the homogenous mixture assumption, (2) thermodynamic relations for the phase mixture are not considered within the employed (R-P equation-based) liquid-vapor mass transfer model, (3) cavitation-induced gas release is not captured, since only pure vapor and gas bubbles are being modelled, (4) gas desorption and absorption is modeled ad hoc based on the difference between local partial gas pressure and its equilibrium pressure based on the amount of dissolved gas, and (5) the critical pressure of the liquid is set to equal its vapor pressure without considering the influence of viscous normal stresses. To demonstrate the consistency of our numerical results with prior numerical work on this specific orifice geometry, Figure 15 also includes results presented by Coussirat et al. [46] based on a SST  $k-\omega$  turbulence model and the cavitation model by Singhal et al. [30] calibrated for this flow configuration. Note that Coussirat et al. did not find meaningful differences in their results when using the Singhal et al. [30] and the Zwart–Gerber–Belamri model [29]. They did not provide the results of their mesh sensitivity study for this model combination since the effects were reported to be small. We note that their data agree closely with our numerical results, even though their prediction for the static pressure variation at tap 1 does show a slight “kink” at the cavitation number where cavitation onset is observed in our experiments.

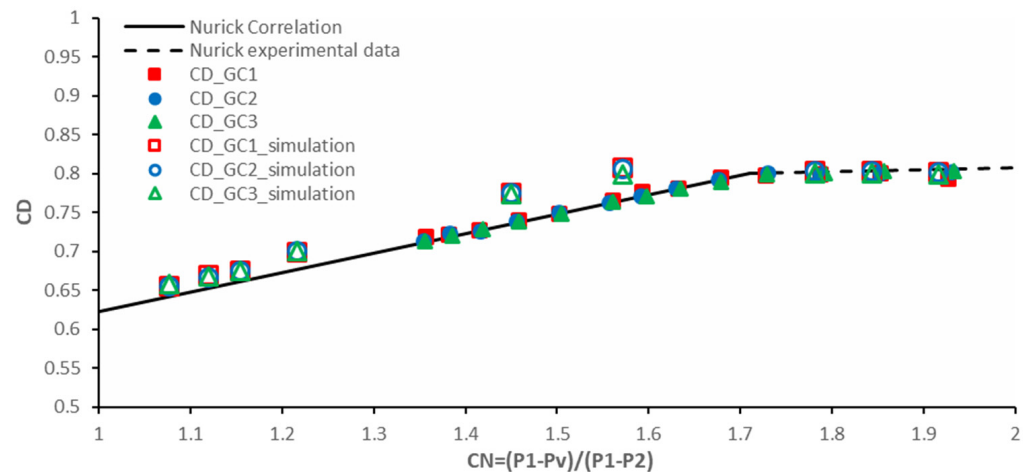


**Figure 15.** Dimensionless cavity pressures  $P_{Cav1,2}$  at pressure taps 1 and 2 as a function of the cavitation number, for two dissolved gas concentrations, i.e., GC1 (left) and GC3 (right). Comparison between experimental (black) and numerical (blue) results. Also shown are simulation results by Coussirat et al. [46].

Figure 16 shows a comparison of the orifice discharge coefficients  $C_d$  predicted using our CFD simulations for the three considered dissolved gas contents (i.e., GC1, GC2, and GC3) with those obtained from our experiments (see also Figure 13). Also presented are Nurick’s data [14], which are already included in Figure 13. Simulation results are found to be in good agreement with our experimental results and Nurick’s data in the non-cavitating case (high  $CN$  values) and also agree well with Nurick’s correlation in the full cavitation zone ( $CN < 1.3$ ). However, the simulations predict cavitation onset at smaller cavitation numbers (see also Figure 15 in this context), resulting in an overprediction of the discharge coefficient in the respective range of cavitation numbers. Similar observations were also made by Singhal et al. [30] and Lifante and Frank [44]. Darbandi et al. [42] and Coussirat et al. [46], using the cavitation model by Singhal et al. [30] and a  $k-\omega$  and SST  $k-\omega$  turbulence model, respectively, do not find this overprediction; however, their  $C_d$  values at higher cavitation numbers are underpredicted.

Similar to our experimental observations, the simulations do not show a meaningful reduction in the discharge coefficient with an increase in dissolved  $CO_2$  content from GC1 to GC2. For case GC3, a reduction in the discharge coefficient is only predicted for the data point at  $CN = 1.57$ , whereas in the experimental data, a reduction is observed over a broader  $CN$  value range; see Figure 13.

Since most prior published work on this flow geometry was carried out with water containing dissolved air (or untreated water) in lieu of dissolved  $\text{CO}_2$ , numerical simulations and experimental flow visualizations were also carried out for three select cases, representative of three cavitation numbers (at or near the onset of cavitation and full cavitation) and with a dissolved air mass fraction of 15 ppm. This latter value corresponds to the value employed in the analyses by Singhal et al. [30], Lifante and Frank [44], and Darbandi et al. [42]. Findings for these cases with dissolved air were found to correspond to those discussed in the context of our study of dissolved  $\text{CO}_2$  and specifically with low amounts of dissolved  $\text{CO}_2$  (i.e., cases GC1 and GC2 according to Table 1).

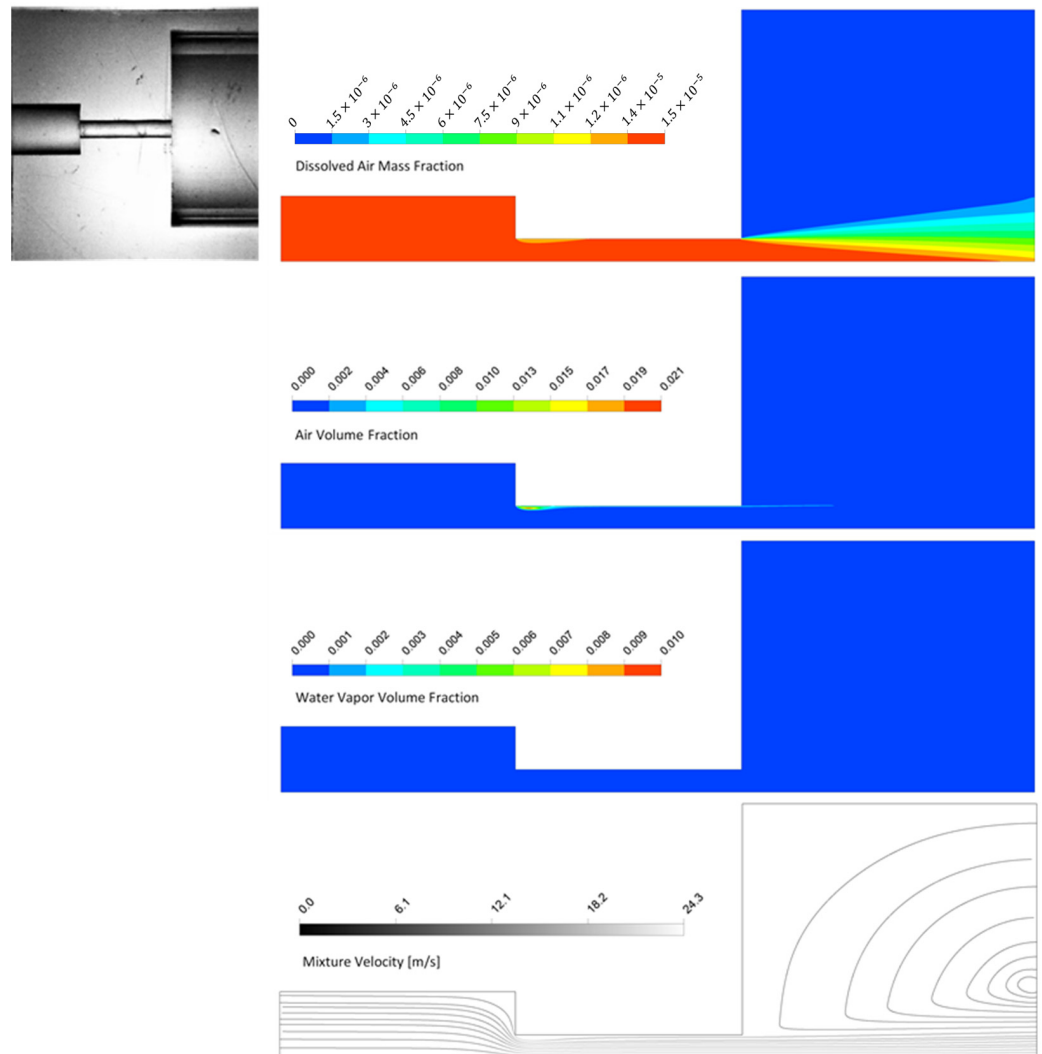


**Figure 16.** Discharge coefficient as a function of the cavitation number based on experimental results, correlation by Nurick [14], and CFD simulation results based on the full cavitation model.

Figures 17–19 illustrate computed results for the prescribed cases with dissolved air together with the respective experimental observations over the entire flow domain, i.e., including both the orifice region and the downstream expanded flow section. The overall development of the cavitation and outgassing phenomena is captured reasonably well using the employed model (see Section 4) at low dissolved gas content, even though quantitative differences exist. Figure 17 illustrates the point of cavitation inception within the experiment, taking place at cavitation number  $CN = 2.13$ . In the respective simulation, cavitation has not yet occurred. However, air is evolving out of the liquid phase, albeit only at a small rate. This conforms to the experimental result, which does not yet show the appearance of air bubbles in the expanded downstream section. It is important to note that the zero values of dissolved gas content in the expanded downstream section result from the established large recirculation zone surrounding the discharging orifice jet (see the streamline plot in Figure 17) and the imposed outlet pressure condition, allowing only pure liquid water, i.e., with zero dissolved air content, to re-enter the domain. With an increase in inlet pressure (i.e., a decrease in cavitation number), cavitation becomes stronger.

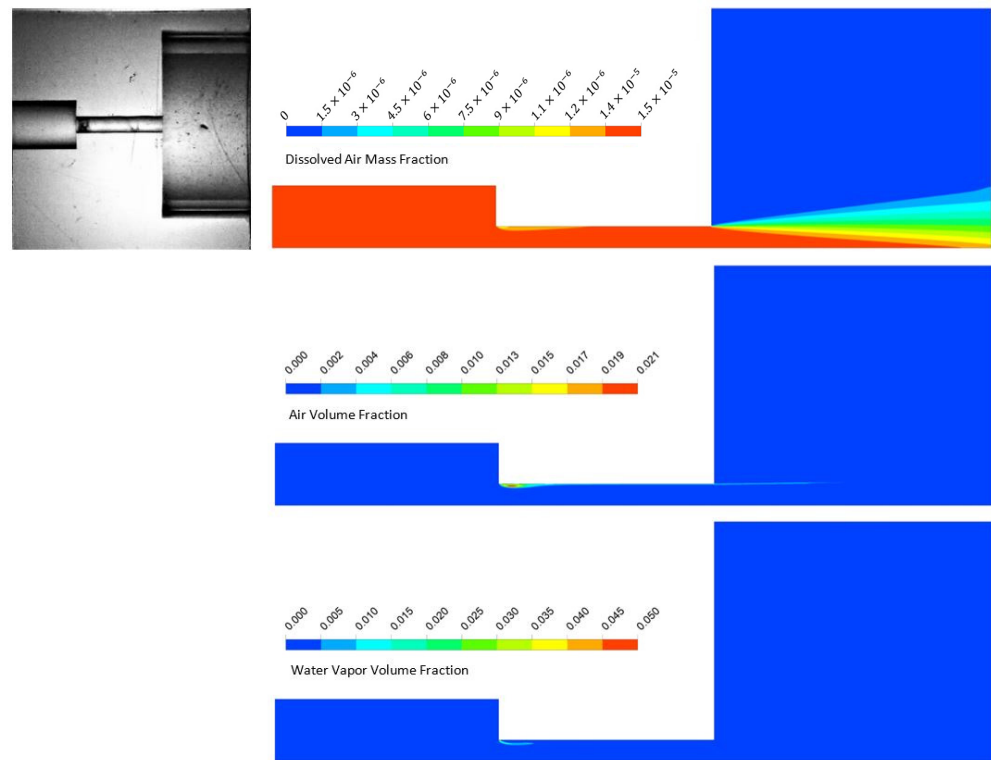
Figure 18 illustrates the case for  $CN = 1.85$ ; this represents the value at which cavitation inception is predicted using the simulation model (see also Figure 15 for case CG1). Cavitation takes place in the shear layer between the core flow and the flow recirculation zone after the contraction. Surprisingly, the axial extent of the predicted cavitation zone is close to that found experimentally. Parallel to vapor cavitation, outgassing is predicted to occur now at a higher rate, whereby the free air remains confined to the recirculation zone near the vena contracta, the downstream orifice wall, and the shear layer of the discharging orifice jet. This conforms to the appearance of microbubbles in the expanded downstream section within the experiment. With a further reduction in the cavitation number, the rate of vapor cavitation increases, and the cavitating flow zone starts to expand downstream while the air outgassing rate also increases. At  $CN = 1.55$ , as illustrated in Figure 19, full cavitation is observed in the experiment, i.e., the cavitating flow region extends over the

entire length of the orifice and up to the downstream expansion zone. The streaky bright and dark areas are indicative of the existence of single-phase areas containing pure gas or vapor and areas with finely dispersed gas/vapor bubbles. In addition, significantly more bubbles are observed in the expanded flow region downstream. In the respective numerical solution, the cavitating flow region has not yet reached the entire length of the orifice. However, for a length of about two orifice diameters downstream of the contraction, the wall region is filled with only vapor (vapor volume fraction equal to 1). Further downstream, the wall region is occupied by air evolved out of the liquid phase, which subsequently discharges with the core jet into the expanded downstream flow region. The air outgassing rate has now grown to approximately three times that predicted for  $CN = 2.13$ . A quantitative comparison with experimentally determined released air volume rates has not been carried out.

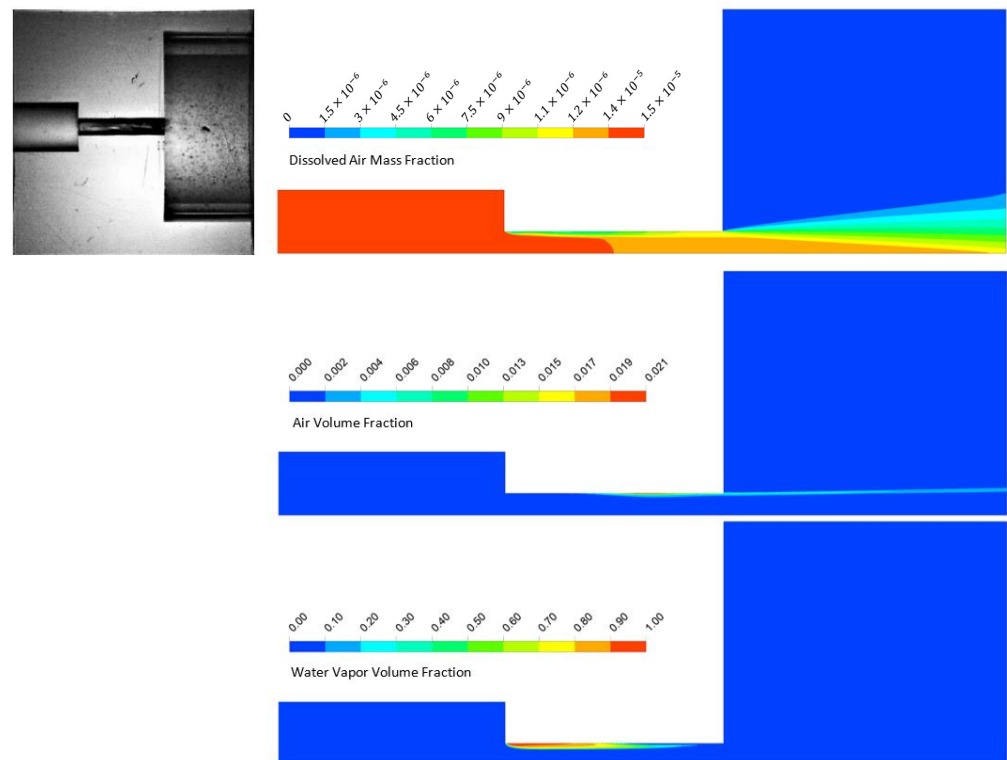


**Figure 17.** Comparison of simulation results with experimental observations at  $CN = 2.13$ , corresponding to the experimentally observed cavitation onset. Operating fluid: tap water with 15 ppm dissolved air mass fraction. Also shown are backward-traced streamlines beginning at the flow outlet. Gas content in the recirculation region of the extended outlet is zero since inflow from that boundary is set to be pure water. Flow direction from left to right.





**Figure 18.** Comparison of simulation results with experimental observations for a similar case as in Figure 17 but at  $CN = 1.85$ , corresponding to cavitation onset in the numerical prediction. Flow direction from left to right.



**Figure 19.** Comparison of simulation results with experimental observations for a similar case as in Figure 17 but at  $CN = 1.55$ , corresponding to experimentally observed full cavitation. Flow direction from left to right.

## 6. Summary

The effect of dissolved gases on the inception and evolution of vapor cavitation was investigated for the well-known sharp-edged orifice geometry already analyzed by Nurick [14], who did not consider the influence of dissolved gases. Water with five different concentrations of dissolved CO<sub>2</sub> was prepared. In the present setup and in contrast to Nurick's configuration, the flow does not discharge into a gas-filled vessel but discharges into an expanding flow section from which it continues to flow downstream. Mass flow through the orifice was controlled by adjusting the pressure in the upstream vessel containing the prepared water volume while the downstream pressure was held constant. The test article was made of PMMA, and backlighting was used to observe the orifice flow using a high-speed camera. Cavitation inception for five different carbon dioxide contents was detected by visual observation and by measuring changes in wall-static pressures (at distances  $d/4$  and  $d/2$  downstream of the orifice edge) with changes in the cavitation number. Comparing visual observations with recorded pressure data shows that, except for the case with the highest dissolved CO<sub>2</sub> content onset of cavitation coincides with a plateau formation in the variation of wall pressures with the cavitation number. A similar observation was already made by Nurick [14]; however, in the present case, the plateau formation is more pronounced and is also found at the pressure tab closest to the orifice edge.

The experimental results show that an increase in dissolved CO<sub>2</sub> concentration leads to higher cavitation numbers at which cavitation inception occurs. Outgassing, i.e., the desorption of dissolved gas from the liquid phase, was found to occur at higher cavitation numbers and before the onset of vapor cavitation. Evidence of outgassing was provided by the appearance of gas bubbles in the downstream expanded flow section and in the channels of the wall-static pressure tabs, the latter being situated in the recirculation region near the vena contracta.

For low dissolved CO<sub>2</sub> content, discharge coefficients from the current measurements agree well with those presented by Nurick [14], even though the amount of dissolved CO<sub>2</sub> changes the cavitation number  $CN$  at which cavitation inception occurs. At higher dissolved gas content, gas evolution is increased at the same  $CN$  number (which might also significantly enhance vapor cavitation), and the evolved gas (and additional vapor) fraction leads to a further blockage of the flow cross-section for the liquid phase, thereby leading to a notable drop in discharge coefficient. At low  $CN$  numbers, i.e., at full cavitation conditions, the amount of dissolved CO<sub>2</sub> is found to have no impact on the discharge coefficient.

CFD analyses for the orifice flow have been carried out using the cavitation model by Zwart et al. [29] and the model by Yang et al. [45] to account for non-condensable gas. Numerical results for three dissolved CO<sub>2</sub> mass fractions, as well as a selected number of cases with dissolved air in lieu of CO<sub>2</sub> (at a mass fraction of 15 ppm) were obtained. Predictions for cases with a low CO<sub>2</sub> mass fraction and those with dissolved air follow the results predicted by other authors using similar models and 15 ppm of dissolved air. An agreement was found in terms of discharge coefficient as a function of cavitation number  $CN$  and in the case of Coussirat et al. [46] also in terms of dimensionless wall pressure predictions with variation in  $CN$  values.

In the numerical simulations, the onset of vapor cavitation is predicted to occur at lower cavitation numbers than found experimentally, irrespective of the amount of dissolved CO<sub>2</sub> gas. The experimental observation that the onset of cavitation occurs at larger cavitation numbers with increased dissolved CO<sub>2</sub> content is not reflected in the numerical results. On the contrary, the simulations predict that cavitation occurs at smaller cavitation numbers with an increase in dissolved CO<sub>2</sub> content. Also, the plateau observed in the variation of static wall pressure tab values with changes in the cavitation number found at the onset of cavitation is not captured using the present numerical simulations.

The present investigation has augmented the experimental data set for the orifice geometry previously investigated by Nurick by including information on the effect of non-condensable dissolved gas (specifically carbon dioxide) on flow cavitation. The new data

can serve for the validation of advanced cavitation models, which are able to capture the complex interaction of the vapor cavitation and outgassing (i.e., gas cavitation) phenomena.

**Author Contributions:** Conceptualization, C.M.; Methodology, S.S.; Software, S.S.; Validation, S.S.; Formal analysis, C.M.; Investigation, S.S.; Writing—original draft, S.S.; Writing—review & editing, C.M.; Visualization, S.S.; Supervision, C.M.; Project administration, C.M.; Funding acquisition, C.M. All authors have read and agreed to the published version of the manuscript.

**Funding:** This research received no external funding.

**Data Availability Statement:** Data are contained within the article.

**Conflicts of Interest:** The authors declare no conflict of interest.

### Appendix A

In this appendix, we briefly review the model equations employed to produce the numerical results presented in this work. Numerical simulations were carried out using the commercial flow-solver ANSYS CFX together with the mass transfer models for vapor (i.e., vapor cavitation) and non-condensable gases (i.e., pseudo cavitation) as previously presented by Zwart et al. [29] and Yang et al. [45] and later referenced by Lifante and Frank [44]. The working fluid is a three-phase mixture consisting of gaseous carbon dioxide, water vapor, and liquid water, which itself is considered a two-component liquid composed of pure water and dissolved carbon dioxide. The homogenous mixture assumption is employed, and all phases share the same velocity and pressure field. The mass transport equation for each phase  $k$ , i.e., liquid water ( $k = l$ ), water vapor ( $k = v$ ), and gaseous CO<sub>2</sub> ( $k = g$ ) reads:

$$\frac{\partial(\alpha_k \rho_k)}{\partial t} + \frac{\partial(\alpha_k \rho_k u_i)}{\partial x_i} = \dot{S}_k \tag{A1}$$

in the absence of a relative velocity between phase  $k$  and the mixture [56]; where  $\alpha_k$  denotes the phase volume fraction of phase  $k$ ,  $\rho_k$  its density,  $u_i$  is the velocity component of the mixture and  $\dot{S}_k$  the mass transfer rate of phase  $k$  due to phase transition. For the dissolution of CO<sub>2</sub> in water, it is assumed that the liquid phase volume does not change despite increasing its mass [50].

Based on conservation principles, we have:

$$\sum_k \alpha_k = 1. \tag{A2}$$

In addition,  $Y_w + Y_{D,g} = 1$  for the liquid phase where  $Y_w$  and  $Y_{D,g}$  denote the mass fractions of pure water and dissolved CO<sub>2</sub>, respectively. For determining the local mass fraction of dissolved CO<sub>2</sub> in the liquid phase, an additional mass transport equation is solved, i.e.,

$$\frac{\partial}{\partial t} (\alpha_l \rho_l Y_{D,g}) + \nabla \cdot ((\alpha_l \mathbf{u} \rho_l Y_{D,g}) - (\alpha_l \rho_l D_g (\nabla Y_{D,g}))) = -\dot{S}_g \tag{A3}$$

where  $D_g$  denotes the diffusivity of dissolved CO<sub>2</sub> in pure water. Conservation of momentum equations for the mixture is given by

$$\frac{\partial(\rho_m u_i)}{\partial t} + \frac{\partial(\rho_m u_i u_j)}{\partial x_j} = -\frac{\partial p}{\partial x_i} + \frac{\partial(\tau_{ij})}{\partial x_j} + \rho_m g_i, \tag{A4}$$

where  $p$  is the pressure,  $\tau_{ij}$  the components of the stress tensor, and  $g_i$  the directional component of gravitational acceleration. Mixture density  $\rho_m$  is given by

$$\rho_m = \sum_k \alpha_k \rho_k, \tag{A5}$$

where the density of each phase was assumed to be constant in the present investigation (and the liquid density was assumed to be that of pure water irrespective of the amount of dissolved gas); in this case, the velocity divergence balances the volume generation due to phase change (see [29]). Components of the stress tensor are evaluated based on Stokes' hypothesis, i.e.,

$$\tau_{ij} = \mu_m \left[ \left( \frac{\partial u_i}{\partial x_j} + \frac{\partial u_j}{\partial x_i} \right) - \frac{2}{3} \delta_{ij} \frac{\partial u_k}{\partial x_k} \right] \tag{A6}$$

and with the molecular viscosity of the mixture  $\mu_m$  calculated as a volume-weighted average analogous to the mixture density, i.e.,

$$\mu_m = \sum_k \alpha_k \mu_k. \tag{A7}$$

For turbulent flows, as considered here, the velocity components in the above equations represent time-averaged quantities, i.e., after averaging the local velocity on the time scale of the turbulent fluctuations (Reynolds averaging). Based on Boussinesq's hypothesis, the additional stress terms (Reynolds stresses) appearing in Equation (A4), in this case, can be modeled by adding an eddy viscosity  $\mu_t$  to the value of the molecular viscosity  $\mu_m$  in Equation (A7). Here, we employ the two-equation  $k-\omega$  SST turbulence model to express  $\mu_t$  based on the density of the mixture; see also [50].

For calculating the mass transfer source terms due to cavitation and condensation in Equation (A1), the model by Zwart et al. [29] is employed. The model is derived from a simplified version of the Rayleigh–Plesset equation (neglecting second-order terms and surface tension in the equation). It neglects bubble interaction but considers the effect of vapor volume fraction on nucleation site density. The respective source terms for the liquid and vapor phase in Equation (A1) are

$$\dot{S}_v = -\dot{S}_l = \begin{cases} F_{vap} \frac{3\alpha_{nuc}(1-\alpha_v) \rho_v}{R_{nuc}} \sqrt{\frac{2}{3} \left( \frac{p_v - p}{\rho_l} \right)} & \text{for } p < p_v \\ F_{cond} \frac{3\alpha_v \rho_v}{R_{nuc}} \sqrt{\frac{2}{3} \left( \frac{p_v - p}{\rho_l} \right)} & \text{for } p > p_v \end{cases} \tag{A8}$$

with the model parameters  $F_{vap} = 50$  and  $F_{cond} = 0.01$  and where  $R_{nuc}$  is the nuclei radius set to be  $2 \times 10^{-6}$  m in the present investigation.

The model assumes that the breaking strength of the liquid is reached when the pressure (also referred to as the critical pressure  $p_{cr}$ ) reaches the vapor pressure  $p_v$ . However, viscous normal stresses might have to be considered [57] in determining  $p_{cr}$  [58] and improved results might be obtained by replacing  $p_v$  in Equation (A8) above by the respective  $p_{cr}$  value, i.e.,

$$p_{cr} = p_v + 2 (\mu_m + \mu_t) T_{ij}^{max}, \tag{A9}$$

where  $T_{ij}^{max}$  denotes the maximum principal component of the strain-rate tensor. However, the present investigation assumes  $p_{cr} = p_v$ .

Following Yang et al. [45], the mass transfer source term  $\dot{S}_g$  due to gas desorption and absorption in Equations (A1) and (A3), can be written as the sum of a desorption term  $R_{des}$  and an absorption term  $R_{abs}$ , i.e.,

$$\dot{S}_g = R_{des} - R_{abs} \tag{A10}$$

with absorption and desorption being driven by the difference between the local partial pressure of the non-condensable gas in its gaseous state and its equilibrium pressure based on the amount of gas dissolved in the liquid. This is different from Rayleigh–Plesset-equation-based models, where the phase change rates are governed by a square-root dependence of pressure difference. Considering that no desorption is possible if there is no liquid phase locally (i.e.,  $\alpha_g = 1$ ) or no dissolved gas content (i.e.,  $Y_{D,g} = 0$ ) and similarly

considering that no gas absorption is possible if there is no free gas locally (i.e.,  $\alpha_g = 0$ ) or the liquid phase is saturated with dissolved gas already; the formulas for evaporation and condensation rates according to Yang et al. [45] can be written as follows:

$$R_{abs} = C_a \rho_g (p - p_{equil}) \left( f_{g, l, lim} - Y_{D,g} \frac{\rho_l \alpha_l}{\rho_m} \right) \frac{\rho_g \alpha_g}{\rho_m}, \tag{A11}$$

$$R_{des} = C_d \rho_g (p_{equil} - p) \left( 1.0 - \frac{\rho_g \alpha_g}{\rho_m} \right) Y_{D,g} \frac{\rho_l \alpha_l}{\rho_m}. \tag{A12}$$

Here,  $p_{equil}$  denotes the sum of liquid/water vapor pressure and the equilibrium gas-phase pressure  $p_g$  based on the dissolved gas fraction in the liquid, i.e.,

$$p_{equil} = p_v + p_g \tag{A13}$$

with  $p_g$  evaluated using Henry’s law

$$p_g = H_v^{px} X_{D,g}. \tag{A14}$$

In this equation,  $H_v^{px}$  denotes the Henry volatility constant and

$$X_{D,g} = \left( \frac{M_l}{M_g} \right) Y_{D,g} \tag{A15}$$

is the mole fraction of dissolved gas.  $C_a$  and  $C_D$  in the prior equations are empirical constants and  $f_{g, l, lim}$  denotes the maximum solubility value of the non-condensable gas (i.e., CO<sub>2</sub> in the present investigation) written in terms of its local overall mass fraction. Here, we have chosen  $C_a = 0.1$  and  $C_D = 2$ , corresponding to the values proposed by Yang et al. [45] for orifice flows. In order to consider the effect of turbulent pressure fluctuations on the threshold pressure below which phase change phenomena occur, the value of vapor pressure  $p_v$  in the above model equations was increased by the local turbulent pressure fluctuation [45], i.e.,

$$p_v = p_{sat} + p'_{turb} \tag{A16}$$

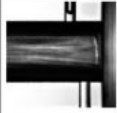


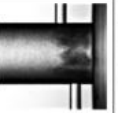

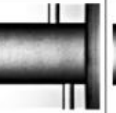
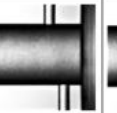

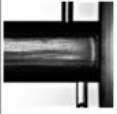




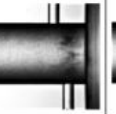
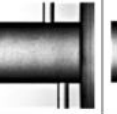






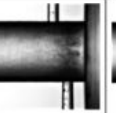
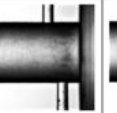






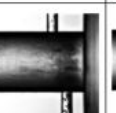
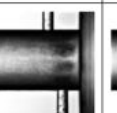

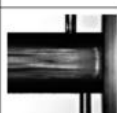




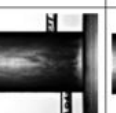


where  $p_{sat}$  refers to the vapor (or saturation) pressure without turbulence effects and

$$p'_{turb} = 0.39(1 - \alpha_v)\rho_l k \tag{A17}$$

with  $k$  denoting the local turbulent kinetic energy. The expression for  $p'_{turb}$  corresponds to that proposed by Yang et al. but with the corrective factor  $(1 - \alpha_v)$  as proposed by Lifante and Frank [44].

### Appendix B

The second set of test data and respective visual observations from the experimental test campaign for similar conditions is presented in Figure 10 but with a frame of view more focused on the flow area after the contraction. Flow direction from right to left.

|                                |   |   |   |   |   |  |   |   |
|--------------------------------|---|---|---|---|---|--|---|---|
| Cavitation Number, CN          | 1.68  | 1.73  | 1.79  | 1.85  | 1.93  | 2.02   | 2.13  | 2.27  |
| GC1                            |    |    |    |    |    |    |    |    |
| Length of cavitation zone [mm] | Transition to full cavitation   | 3.22  | 2.23  | 1.64  | 1.31  | 0  | 0   | 0   |
| Cavitation Number, CN          | 1.68  | 1.73  | 1.79  | 1.85  | 1.93  | 2.02   | 2.13  | 2.27  |
| GC2                            |    |    |    |    |    |    |    |    |
| Length of cavitation zone [mm] | full cavitation   | Transition to full cavitation   | 2.92  | 2.06  | 1.63  | 1.35   | 0   | 0   |
| Cavitation Number, CN          | 1.68  | 1.73  | 1.79  | 1.86  | 1.93  | 2.03   | 2.14  | 2.28  |
| GC3                            |    |    |    |    |    |    |    |    |
| Length of cavitation zone [mm] | Full cavitation   | Transition to full cavitation   | 4.22  | 2.92  | 1.96  | 1.50   | 1.33  | 0   |
| Cavitation Number, CN          | 1.69  | 1.74  | 1.80  | 1.86  | 1.94  | 1.96   | 2.07  | 2.20  |
| GC4                            |  |  |  |  |  |  |  |  |
| Length of cavitation zone [mm] | Full cavitation   | Full cavitation   | Transition to full cavitation   | 4.10  | 3.27  | 2.22   | 1.56  | 1.31  |
| Cavitation Number, CN          | 1.69  | 1.74  | 1.80  | 1.87  | 1.94  | 2.04   | 2.15  | 2.29  |
| GC5                            |  |  |  |  |  |  |  |  |
| Length of cavitation zone [mm] | Full cavitation   | Full cavitation   | Full cavitation   | 4.90  | 4.44  | 3.69   | 2.82  | 2.05  |

**Figure A1.** Flow observations from second set of test data for broad range of cavitation numbers  $CN$  and 5 different mass fractions of dissolved  $CO_2$ , i.e., GC1–GC5 according to Table 1. Flow direction from right to left. Results are comparable to those presented in Figure 10.

## References

- Brennen, C. *Cavitation and Bubble Dynamics*; Cambridge University Press: Cambridge, UK, 2013.
- Brennen, C. *Fundamentals of Multiphase Flow*; Cambridge University Press: Cambridge, UK, 2005.
- Franc, J.-P.; Michel, J.-M. Fundamentals of Cavitation. In *Fluid Mechanics and Its Applications*; Moreau, R., Ed.; Springer Science & Business Media: Dordrecht, The Netherlands, 2005.
- Perk, O.Y.; Şeşen, M.; Gozuacik, D.; Koşar, A. Kidney stone erosion by micro scale hydrodynamic cavitation and consequent kidney stone treatment. *Ann. Biomed. Eng.* **2012**, *40*, 1895–1902. [[CrossRef](#)]
- Zijlstra, A.G. Acoustic Surface Cavitation. Ph.D. Dissertation, University of Twente, Enschede, The Netherlands, 2011.
- Vasile, E.; Ciocanea, A.; Ionescu, V.; Lepadatu, I.; Diac, C.; Stamatini, S.N. Making precious metals cheap: A sonoelectrochemical–Hydrodynamic cavitation method to recycle platinum group metals from spent automotive catalysts. *Ultrason. Sonochem.* **2021**, *72*, 105404. [[CrossRef](#)]

7. Kim, M.; Kim, D.; Cho, J.M.; Nam, K.; Lee, H.; Nayak, M.; Han, J.; Oh, H.-M.; Chang, Y.K. Hydrodynamic cavitation for bacterial disinfection and medium recycling for sustainable *E. coli* sp. Cultivation. *J. Environ. Chem. Eng.* **2021**, *9*, 105411. [[CrossRef](#)]
8. Kosel, J.; Šuštaršič, M.; Petkovšek, M.; Zupanc, M.; Sežun, M.; Dular, M. Application of (super) cavitation for the recycling of process waters in paper producing industry. *Ultrason. Sonochemistry* **2020**, *64*, 105002. [[CrossRef](#)] [[PubMed](#)]
9. Song, Y.; Hou, R.; Zhang, W.; Liu, J. Hydrodynamic cavitation as an efficient water treatment method for various sewage: A review. *Water Sci. Technol.* **2022**, *86*, 302–320. [[CrossRef](#)]
10. Gogate, P.R.; Pandit, A.B. Cavitation generation and usage without ultrasound: Hydrodynamic cavitation. *Theor. Exp. Sonochem. Involv. Inorg. Syst.* **2011**, 69–106. [[CrossRef](#)]
11. Li, B.; Gu, Y.; Chen, M. An experimental study on the cavitation of water with dissolved gases. *Exp. Fluids* **2017**, *58*, 164. [[CrossRef](#)]
12. Mehring, C. Liquid-Fuel Ejector Pump under Multiphase-Flow Conditions. In Proceedings of the 25th European Conference on Liquid Atomization and Spray Systems, Chania, Greece, 1–4 September 2013.
13. Zheng, H.; Zheng, Y.; Zhu, J. Recent developments in hydrodynamic cavitation reactors: Cavitation mechanism, reactor design, and applications. *Engineering* **2022**, *19*, 180–198. [[CrossRef](#)]
14. Nurick, W.H. Orifice cavitation and its effect on spray mixing. *J. Fluids Eng.* **1976**, *98*, 681–687. [[CrossRef](#)]
15. Arakeri, V.H. Cavitation inception. *Proc. Indian Acad. Sci. Sect. C Eng. Sci.* **1979**, *2*, 149–177. [[CrossRef](#)]
16. Nurick, W.H.; Ohanian, T.; Talley, D.G.; Strakey, P.A. Impact of L/D on 90 Degree Sharp-Edge Orifice Flow with Manifold Passage Cross Flow (Preprint). *J. Artic.* **2007**, *30*, 2.
17. Yan, Y.; Thorpe, R.B. Flow regime transitions due to cavitation in the flow through an orifice. *Int. J. Multiph. Flow* **1990**, *16*, 1023–1045. [[CrossRef](#)]
18. Mishra, C.; Peles, Y. Cavitation in flow through a micro-orifice inside a silicon microchannel. *Phys. Fluids* **2005**, *17*, 013601. [[CrossRef](#)]
19. Zhang, H.; Zuo, Z.; Liu, S. Influence of Dissolved Gas Content on Venturi Cavitation at Thermally Sensitive Conditions. In Proceedings of the 10th International Symposium on Cavitation (CAV2018), Baltimore, MD, USA, 14–16 May 2018; pp. 546–550.
20. Rooze, J. Cavitation in Gas-Saturated Liquids. Ph.D. Thesis, Eindhoven University of Technology, Eindhoven, The Netherlands, 2012.
21. Freudigmann, H.A.; Dörr, A.; Iben, U.; Pelz, P.F. Modeling of cavitation-induced air release phenomena in micro-orifice flows. *J. Fluids Eng.* **2017**, *139*, 111301. [[CrossRef](#)]
22. Kowalski, K.; Pollak, S.; Skoda, R.; Hussong, J. Experimental study on cavitation-induced air release in orifice flows. *ASME J. Fluids Eng.* **2018**, *140*, 061201. [[CrossRef](#)]
23. Duke, D.; Kastengren, A.L.; Tilocco, F.Z.; Swantek, A.B.; Powell, C.F. X-ray radiography measurements of cavitating nozzle flow. *At. Sprays* **2013**, *23*. [[CrossRef](#)]
24. Duke, D.J.; Swantek, A.B.; Kastengren, A.L.; Powell, C.F. X-ray diagnostics for cavitating nozzle flow. *J. Phys. Conf. Ser.* **2015**, *656*, 012110. [[CrossRef](#)]
25. Duke, D.J.; Matusik, K.E.; Kastengren, A.L.; Swantek, A.B.; Sovis, N.; Payri, R.; Viera, J.P.; Powell, C.F. X-ray radiography of cavitation in a beryllium alloy nozzle. *Int. J. Engine Res.* **2017**, *18*, 39–50. [[CrossRef](#)]
26. Sou, A.; Biçer, B.; Tomiyama, A. Numerical simulation of incipient cavitation flow in a nozzle of fuel injector. *Comput. Fluids* **2014**, *103*, 42–48. [[CrossRef](#)]
27. Schnerr, G.H.; Sauer, J. Physical and Numerical Modeling of Unsteady Cavitation Dynamics. In Proceedings of the Fourth International Conference on Multiphase Flow (Vol. 1), New Orleans, LO, USA, 27 May–1 June 2001.
28. Kunz, R.F.; Boger, D.A.; Stinebring, D.R.; Chyczewski, T.S.; Lindau, J.W.; Gibeling, H.J.; Venkateswaran, S.; Govindan, T.R. A preconditioned Navier–Stokes method for two-phase flows with application to cavitation prediction. *Comput. Fluids* **2000**, *29*, 849–875. [[CrossRef](#)]
29. Zwart, P.J.; Gerber, A.G.; Belamri, T. A Two-Phase Flow Model for Predicting Cavitation Dynamics. In Proceedings of the Fifth International Conference on Multiphase Flow, Yokohama, Japan, 30 May–4 June 2004; p. 152.
30. Singhal, A.K.; Athavale, M.M.; Li, H.; Jiang, Y. Mathematical basis and validation of the full cavitation model. *ASME J. Fluids Eng.* **2002**, *124*, 617–624. [[CrossRef](#)]
31. Battistoni, M.; Som, S.; Longman, D.E. Comparison of mixture and multifluid models for in-nozzle cavitation prediction. *J. Eng. Gas Turbines Power* **2014**, *136*, 061506. [[CrossRef](#)]
32. Li, W.; Yu, Z. Cavitation models with thermodynamic effect for organic fluid cavitating flows in organic Rankine cycle systems: A review. *Therm. Sci. Eng. Prog.* **2021**, *26*, 101079. [[CrossRef](#)]
33. Battistoni, M.; Duke, D.; Swantek, A.B.; Tilocco, F.Z.; Powell, C.F.; Som, S. Effects of noncondensable gas on cavitating nozzles. *At. Sprays* **2015**, *25*. [[CrossRef](#)]
34. Yang, S.; Habchi, C. Real-fluid phase transition in cavitation modeling considering dissolved non-condensable gas. *Phys. Fluids* **2020**, *32*, 032102. [[CrossRef](#)]
35. Amini, A.; Reclari, M.; Sano, T.; Farhat, M. Effect of Gas Content on Tip Vortex Cavitation. In Proceedings of the 10th International Symposium on Cavitation (CAV2018), Baltimore, MD, USA, 14–16 May 2018.
36. Mukherjee, S.; Gomez, H. Effect of dissolved gas on the tensile strength of water. *Phys. Fluids* **2022**, *34*, 126112. [[CrossRef](#)]
37. Iben, U.; Makhnov, A.; Schmidt, A. Numerical study of the effects of dissolved gas release in cavitating flow. *AIP Conf. Proc.* **2018**, *2027*, 030128.

38. Iben, U.; Makhnov, A.; Schmidt, A. Numerical study of dissolved gas release induced by cavitation in a high speed channel flow. *J. Phys. Conf. Ser.* **2019**, *1400*, 077037. [[CrossRef](#)]
39. Malekshah, E.H.; Wróblewski, W. Merging theory-based cavitation model adaptable with non-condensable gas effects in prediction of compressible three-phase cavitating flow. *Int. J. Heat Mass Transf.* **2022**, *196*, 123279. [[CrossRef](#)]
40. Richards, K.; Senecal, P.; Pomraning, E. *Converge 2.1.0 Theory Manual*; Convergent Science Inc.: Middleton, WI, USA, 2013.
41. Bohbot, J.; Gillet, N.; Benkenida, A. IFP-C3D: An unstructured parallel solver for reactive compressible gas flow with spray. *Oil Gas Sci. Technol.-Rev. De L'ifp* **2009**, *64*, 309–335. [[CrossRef](#)]
42. Darbandi, M.; Sadegh, H.; Schneider, G.E. Simulating Orifice Cavitation Using the Full Cavitation Model. In Proceedings of the 17th Annual Conference of the CFD Society of Canada, Ottawa, ON, Canada, 3–5 May 2009.
43. Darbandi, M.; Sadeghi, H. Numerical simulation of orifice cavitating flows using two-fluid and three-fluid cavitation models. *Numer. Heat Transf. Part A Appl.* **2010**, *58*, 505–526. [[CrossRef](#)]
44. Lifante, C.; Frank, T. *Investigation of Higher Order Pressure Fluctuations and Its Influence on Ship Stern, Taking into Account Cavitation at Propeller Blades*; TR-08-04; ANSYS Germany GmbH: Berlin, Germany, 2008.
45. Yang, H.Q.; Singhal, A.K.; Megahed, M. Industrial two-phase flow CFD—The Full Cavitation Model. *Von Karman Inst. Fluid Dyn. Lect. Ser.* **2005**, *4*.
46. Coussirat, M.; Moll, F.; Cappa, F.; Fontanals, A. Study of Available Turbulence and Cavitation Models to Reproduce Flow Patterns in Confined Flows. *ASME. J. Fluids Eng.* **2016**, *138*, 091304. [[CrossRef](#)]
47. Stanley, C.; Barber, T.; Milton, B.; Rosengarten, G. Periodic cavitation shedding in a cylindrical orifice. *Exp. Fluids* **2011**, *51*, 1189–1200. [[CrossRef](#)]
48. Mauger, C.; Méès, L.; Michard, M.; Azouzi, A.; Valette, S. Shadowgraph, Schlieren and interferometry in a 2D cavitating channel flow. *Exp. Fluids* **2012**, *53*, 1895–1913. [[CrossRef](#)]
49. Saurabh, A. Cavitation in Injectors: A Brief Review of the Diagnostics of Liquid-Vapour Flow Within Injector Nozzles. Simulations and Optical Diagnostics for Internal Combustion Engines. *Curr. Status Way Forw.* **2020**, 85–93. [[CrossRef](#)]
50. Menter, F. Zonal Two Equation kw Turbulence Models for Aerodynamic Flows. In Proceedings of the 23rd Fluid Dynamics, Plasmadynamics, and Lasers Conference, Orlando, FL, USA, 6–9 July 1993; p. 2906.
51. Peterson, F.B. Discussion: “Orifice Cavitation and Its Effect on Spray Mixing” (Nurick, W.H., 1976, ASME J. Fluids Eng., 98, pp. 681–687). *ASME. J. Fluids Eng.* **1977**, *99*, 426. [[CrossRef](#)]
52. Winklhofer, E.; Kull, E.; Kelz, E.; Morozov, A. Comprehensive Hydraulic and Flow Field Documentation in Model Throttle Experiments under Cavitation Conditions. In Proceedings of the ILASS-Europe Conference, Zurich, Switzerland, 2–6 September 2001; pp. 574–579.
53. Martynov, S.; Mason, D.; Heikal, M.R.; Sazhin, S.S.; Gorokhovski, M. Modelling of Cavitation Flow in a Nozzle and Its Effect on Spray Development. In Proceedings of the International Heat Transfer Conference 13, Sydney, Australia, 13–18 August 2006; Begel House Inc.: New York, NY, USA, 2006.
54. *IEC 60770; Transmitters for Use in Industrial-Process Control Systems—Part 1: Methods for Performance Evaluation*. International Electrotechnical Commission: Geneva, Switzerland, 2010.
55. Battino, R.; Clever, H.L. The solubility of gases in liquids. *Chem. Rev.* **1966**, *66*, 395–463. [[CrossRef](#)]
56. Manninen, M.; Taivassalo, V.; Kallio, S. *On the Mixture Model for Multiphase Flow*; Technical Research Center of Finland, VIT Publications 288: Espoo, Finland, 1996.
57. Joseph, D.D. Cavitation and the state of stress in a flowing liquid. *J. Fluid Mech.* **1998**, *366*, 367–378. [[CrossRef](#)]
58. Martynov, S.B.; Mason, D.J.; Heikal, M.R. Effect of Viscous Stress on Cavitation Flow in Nozzles. *J. Fluids Eng.* **2006**, *9*, 2006.

**Disclaimer/Publisher’s Note:** The statements, opinions and data contained in all publications are solely those of the individual author(s) and contributor(s) and not of MDPI and/or the editor(s). MDPI and/or the editor(s) disclaim responsibility for any injury to people or property resulting from any ideas, methods, instructions or products referred to in the content.